Computers and Geotechnics 192 (2026) 107938

Contents lists available at ScienceDirect

Computers and Geotechnics

journal homepage: www.elsevier.com/locate/compgeo

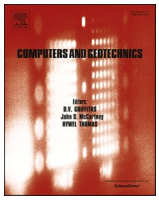

Stochastic simulation of three-dimensional unsaturated flow in water repellent heterogeneous soil

Evan John Ricketts [a,*], Peter John Cleall [a], Anthony Jefferson [a], Pierre Kerfriden [b], Paul Lyons [c]

[a] School of Engineering, Cardiff University, Cardiff CF24 3AA, UK
[b] Centre de Matériaux, Mines Paris /PSL University, Evry, France
[c] LUSAS, Surrey, UK

ARTICLE INFO

Keywords:
Finite element method
Hydrophobicity
Unsaturated soil
Stochastic
Heterogeneity

ABSTRACT

It has been established that spatial variability of material properties can lead to distinct unstable hydraulic behaviour, and that this is prominent in soils due to their large spatial heterogeneity. This characteristic can lead to non-uniform wetting behaviour and is particularly prominent when the wettability of the medium is also non-uniform. In water repellent soil, its wettability is often spatially varying, such that a network of flow paths is created where fluid can move preferentially, leading to fingered flow patterns. In this study, the development of a model to represent moisture transport in hydrophobic soil is presented. Local spatial variations in material properties are represented by Gaussian random fields as part of a stochastic finite element based model. Key components of the model include an approach to represent the transition region between wettable and non-wettable layers, and the adoption of a suitable saturation–capillary pressure relationship. For wettable soil, this can be achieved with the standard van Genuchten relation. For hydrophobic soil, this is not applicable; thus, an alternative is employed. The model is then validated against field-scale experimental observations by Lipsius and Mooney (2006), which examined the impact of soil heterogeneity on infiltration profiles. The results demonstrate the model's ability to capture complex flow dynamics in hydrophobic soils, extending the understanding of moisture transport in heterogeneous soils by explicitly modelling the spatial variability of wettability and its impact on soil hydraulic response.

1. Introduction

With a rapidly changing climate and an increased presence of extreme weather in some regions, there is increased need to understand and quantify the interaction between soil water repellency (WR) and associated hydrological processes. WR in soils can arise naturally from secretion of substances into the root zone (Moradi et al., 2012; Ahmed et al., 2016; Zickenrott et al., 2016), extreme heating due to the presence of wildfire (Cerdà and Doerr, 2008; Bodí et al., 2012; Nyman et al., 2014), or artificially through the use of dimethyldichlorosilane (Bachmann and McHale, 2009; Ng and Lourenço, 2016; Zheng et al., 2019; Saulick and Lourenço, 2020) or wax (Bardet et al., 2014). Hydrophobic soils are problematic in agricultural land as they can lead to lower saturation levels and reduced crop growth. Similarly, the risk of chemicals being transported through runoff is increased, potentially contaminating water sources and causing harm to surrounding wildlife. In some industrial applications, it can be beneficial to employ hydrophobic soils, such as cover systems for landfill sites (Zheng et al., 2021).

The hydrological response of soil with spatially variable levels of wettability is different from that of a soil with uniform wetting properties. When such non-uniformity is pronounced, the surface runoff leads to greater risk of erosion (Granged et al., 2011). Splash and rill erosion also have increased rates, with accelerated rill erosion due to the water repellent layer causing a build-up of pore pressure, and a consequential reduction in shear strength in the overlying saturated soil (DeBano, 2000). In contrast, when the combination of slope angle and rainfall rate allows for a layer of water to form on the surface, rates of erosion could decrease (Lowe et al., 2021). Runoff of this form can be detrimental to the surrounding area, such as flash flooding seen in areas subject to wildfire. It has also been observed that the presence of WR can lead to preferential flow paths, resulting in "fingered flow" (Bauters et al., 1998; Ritsema and Dekker, 2000). Fingers often form due to water

* Corresponding author.
E-mail addresses: rickettse1@cardiff.ac.uk (E.J. Ricketts), cleall@cardiff.ac.uk (P.J. Cleall), jeffersonad@cardiff.ac.uk (A. Jefferson), pierre.kerfriden@minesparis.psl.eu (P. Kerfriden), paul.lyons@lusas.com (P. Lyons).

https://doi.org/10.1016/j.compgeo.2026.107938
Received 24 July 2025; Received in revised form 13 January 2026; Accepted 18 January 2026
Available online 21 January 2026

tracking to areas of higher conductivity, following the path of least resistance. Fingered shapes due to gravity-driven unstable flow have been observed experimentally (Glass et al., 1988; Kawamoto and Miyazaki, 1999; Cremer et al., 2017) This type of flow can also lead to the accelerated transport of chemicals or other solutes present in the fluid phase (Gjettermann et al., 1997; Reichenberger et al., 2002; Morris and Mooney, 2004). Beyond promoting fingered flow, water repellency also modifies conductivity, where dynamic inflow/outflow tests have shown that water retention and hydraulic conductivity are strongly dependent on the degree of repellency, and on whether the process is wetting or drying (Diamantopoulos et al., 2013). Many modelling approaches for soil typically consider the soil to be fully wettable, making it challenging to have a representation of the material that is consistent with non-wettable behaviour. Similarly, even with constitutive components that can represent hydrophobicity, the heterogeneity of the soil properties needs to be accounted for.

Previous modelling studies of fingered flow in water repellent soils have considered hysteresis as a driving factor for the flow dynamics (Nieber, 1996; Nieber et al., 2003). The effects of hysteresis were brought into the solution of the mass balance equation, based on Richard's equation, and was seen to be the cause of persistence in fingered flow. The heterogeneity of the medium was also considered by Ritsema et al., (1998), where the formation and recurrence of fingers were simulated based on a numerical solution comprising coupled water and air flow in a 2-D domain. The authors claimed that the spatial variability of wettability, inferred by a non-homogenous medium, will cause fingers to become permanent preferential pathways. The effects of heterogeneity on finger instability have been further considered by Cueto-Felgueroso et al., (2020), simulating preferential flow during infiltration in a 2-D initially dry heterogeneous soil. Spatial heterogeneity was categorised by spatially correlated random fields −representing intrinsic permeability- allowing for isotropic and anisotropic configurations of permeability to be utilised in the model. The influence of moderate or strong heterogeneity on fingering instability was addressed, concluding that its inclusion enhanced the effects of preferential flow, leading to increased rates of finger development. It was also concluded that the patterns of finger formation strongly depend on the soil structure, namely the correlation length and the covariance kernel of the permeability field. In many cases, it is seen that the heterogeneity of the medium is an influential factor in flow-related processes, suggesting that −in addition to the material variability- representation of the wettability of the medium should also vary spatially.

In this study, an investigation into the modelling of hydrophobic soil is presented. As in the authors' previous work (Ricketts et al., 2023a), local spatial variations in material parameters are accounted for using Gaussian random fields, and a stochastic finite element approach is taken to simulating moisture transport in the WR medium. Whilst various field generation methods exist, such as Karhunen-Loève expansion and covariance matrix decomposition (Li et al., 2019; Montoya-Noguera et al., 2019), the stochastic partial differential equation (SPDE) approach is used here due to its flexibility and ease of inclusion in finite element models (Lindgren et al., 2011; Lindgren et al., 2022). Much of the model development presented here was dedicated to accurately representing the constitutive response of the material, and to exploring the behaviour at the interfaces between soil layers of differing wettabilities. This was necessary because classical soil moisture retention relationships, such as those due to van Genuchten (1980) and Brooks and Corey (1966) are not applicable to WR soils, as explained in Section 3. A further aspect of this study is the explicit consideration of transition zones between WR and wettable layers of soil. The model is applied to replicate a field-scale experiment carried out by Lipsius & Mooney (2006) where infiltration profiles in a WR soil were imaged and evaluated. Results from 3 representative simulations are presented based on the extracted experimental data and quantified using confidence interval calculations.

The layout of the remainder of the paper is as follows: Section 2 describes the theory of the moisture transport solution and random field generation through SPDEs, as well as their numerical solution with the finite element method; Section 3 presents the components of the model that extend its original capabilities such that hydrophobic soils can be modelled effectively; Section 4 explores the application of the model in replicating field-scale experimental observations, addressing the applicability of the results and their uncertainty; and Section 5 presents the main conclusions of the study.

2. Theory and numerical discretisation

2.1. Moisture transport

The theoretical model for moisture transport is based on the approach presented by Cleall et al., (2007), where the soil is assumed to be composed of liquid water and solid mass phases. Here, the influence of the gaseous phase is neglected, meaning that the volumetric water content θ is solely dependent on the liquid phase. The liquid pressure u_l is considered as the primary variable. The volumetric water content is represented by a mass balance equation depending on degree of saturation and porosity, such that

$$\frac{\partial(\rho_l n S_l)}{\partial t} + \rho_l \nabla \bullet \boldsymbol{v_l} = 0 \tag{1}$$

where ρ_l is the liquid density, n the porosity, S_l the degree of saturation of pore water, and $\boldsymbol{v_l}$ the liquid velocity. It is assumed that pressure gradients drive the flow, according to the well-known Darcy's Law (Darcy, 1856; Nielsen et al., 1986; Rosso et al., 2006; Hosseinejad et al., 2019). For flow in unsaturated soils, this is expressed as

$$\boldsymbol{v_l} = -\frac{k_l}{\mu_l}\left[\nabla\left(\frac{u_l}{\gamma_l}\right) + \nabla z\right] = -K_l\left[\nabla\left(\frac{u_l}{\gamma_l}\right) + \nabla z\right] \tag{2}$$

where k_l is the effective permeability, μ_l the pore liquid viscosity, γ_l the unit weight of liquid, z the elevation and K_l the unsaturated hydraulic conductivity. The effects of turbulence in the liquid phase can be neglected due to the assumption that the flow through the medium will be relatively slow.

Here, the unsaturated hydraulic conductivity is assumed to depend on the degree of liquid saturation. The governing equation for the flow of water can now be formulated by combining the mass conservation equation with Darcy's Law, such that

$$C_{ll}\frac{\partial u_l}{\partial l} - \nabla[K_{ll}\nabla u_l] = J_l \tag{3}$$

where

$$C_{ll} = -n\rho_l\frac{\partial S_l}{\partial s}, \quad K_{ll} = \frac{\rho_l K_l}{\gamma_l}, \quad J_l = \rho_l \nabla(K_l \nabla z). \tag{4}$$

Equation (3) is solved using the Finite Element Method. The weak formulation is derived in the usual way, multiplying Equation (3) by a test function $v \in V$ and integrating over the domain Ω, where $V = H^1(\Omega)$ and $\Omega \subset \mathbb{R}^d$. Applying the Gauss-Green divergence theorem yields the following weak form find $u_l \in V$ such that $a(u_l, v) + c\left(\frac{\partial u_l}{\partial t}, v\right) = l(v)$ $\forall v \in V$, where the bilinear forms $a(\cdot,\cdot)$ and $c(\cdot,\cdot)$, and the linear functional $l(\cdot)$ are defined as

$$a(u_l, v) = \int_\Omega K_{ll}\nabla u_l \cdot \nabla \mathbf{v}\, d\Omega$$

$$c\left(\frac{\partial u_l}{\partial t}, v\right) = \int_\Omega C_{ll}\frac{\partial u_l}{\partial t} v\, d\Omega$$

$$l(v) = \int_\Omega K_l \rho_l \nabla v \cdot \nabla z \, d\Omega - \int_\Gamma v[\rho_l \widehat{v}_l] \, d\Gamma \tag{5}$$

where Γ is the domain boundary, and $\widehat{v}_l$ is the approximate liquid velocity normal to the boundary. Following the standard Galerkin finite element approach, we approximate $u_l = \sum_{j=1}^{N_{dof}} u_{l,j} N_j$, where N_j are the basis functions in $H^1(\Omega)$, $u_{l,j}$ are nodal values, and N_{dof} is the total degrees of freedom in Ω. This leads to the matrix equation

$$\mathbf{C}_{ll} \frac{\partial \mathbf{u}_l}{\partial t} + \mathbf{K}_{ll} \mathbf{u}_l = \mathbf{F}_l \tag{6}$$

where the global mass matrix $\mathbf{C}_{ll}$, stiffness matrix $\mathbf{K}_{ll}$, and load vector $\mathbf{F}_l$ are assembled from their element contributions

$$C_{ll,ij} = \int_\Omega C_{ll} N_i N_j d\Omega$$

$$K_{ll,ij} = \int_\Omega K_{ll} \nabla N_i \cdot \nabla N_j \mathrm{d}\Omega$$

$$F_{l,i} = \int_\Omega K_l \rho_l \nabla N_i \cdot \nabla z d\Omega - \int_\Gamma N_i [\rho_l \widehat{v}_l] \, d\Gamma \tag{7}$$

An implicit Euler backward difference scheme is employed for time discretisation (Zienkiewicz et al., 2013), such that

$$\mathbf{K}_{ll} \mathbf{u}_l^{t+1} + \frac{1}{\Delta t} \mathbf{C}_{ll} \left(\mathbf{u}_l^{t+1} - \mathbf{u}_l^t \right) = \mathbf{F}_l \tag{8}$$

To solve the system, the standard Newton-Raphson procedure is applied (Chitez and Jefferson, 2015), and as such, the primary variable is updated incrementally as

$$\delta \mathbf{u}_{l_{k+1}}^{t+1} = \left[\frac{\partial \Psi}{\partial \boldsymbol{u}_{l_k}^{t+1}} \right] (- \Psi) \tag{9}$$

where Ψ is the approximate error given by

$$\Psi = \Delta t \mathbf{K}_{ll} \mathbf{u}_l^{t+1} + \mathbf{C}_{ll} \left(\mathbf{u}_l^{t+1} - \mathbf{u}_l^t \right) - \Delta t \mathbf{F}_l. \tag{10}$$

2.2. Gaussian random field generation

In the following, the theory of random field generation based on the solution of a SPDE is presented (Lindgren et al., 2011; Roininen et al., 2014). Let $\mathbf{X} \in \mathbb{R}^d$ be a Gaussian random field where its contents are parameterised collections of Gaussian random variables $\{\mathbf{X}(\mathbf{x})\}_{\mathbf{x} \in \mathbb{R}^d}$. The covariance of the field is assumed to be a function of spatial distance such that a standard autocorrelation function is suitable in representing the field's correlation structure. Here, the Matérn autocorrelation function is chosen

$$\mathrm{ACF}_X(\mathbf{x}) = \frac{2^{1-\nu}}{\Gamma(\nu)} \left(\frac{|\mathbf{x}|}{l} \right)^\nu K_\nu \left(\frac{|\mathbf{x}|}{l} \right) \tag{11}$$

for $\mathbf{x} \in \mathbb{R}^d$, where $\nu > 0$ is the smoothness parameter, $|\mathbf{x}|$ is the Euclidean distance, Γ is the gamma function, and K_ν is the Bessel function of the second kind of order ν. The length-scale parameter $l > 0$ controls the correlation length of the resulting field, whereby $\delta = l\sqrt{8\nu}$ is the distance for correlations near 0.1 (Lindgren et al., 2011). Following the approach of Roininen et al., (2014), Eq. (11) can be approximated by posing the function as the SPDE

$$\left(1 - l^2 \Delta\right)^{\frac{(\nu + d/2)}{2}} \mathbf{X} = \sqrt{\alpha l^d} \mathbf{W} \tag{12}$$

where $\sqrt{\ }$ denotes the partial Cholesky decomposition, $d = 1, 2, 3$, $\mathbf{W}$ is white noise on $\mathbb{R}^d$, and α is a constant such that

$$\alpha := \sigma^2 \frac{2^d \pi^{d/2} \Gamma(\nu + d/2)}{\Gamma(\nu)} \tag{13}$$

where σ is the standard deviation. The smoothness parameter ν is fixed as $\nu = 2 - d/2$ to render Eq. (12) elliptic, such that

$$\left(\mathbf{I} - l^2 \Delta\right) \mathbf{X} = \sqrt{\alpha l^d} \mathbf{W} \tag{14}$$

where $\mathbf{I}$ is the standard identity matrix. Here, the solution to Eq. (14) is approximated with the finite element method. This is defined over $\mathbb{R}^d$ and has a non-unique solution, and as such, boundary conditions are required such that the problem is well posed. The reduction to a finite domain introduces spurious values in the near-boundary region, resulting in a correlation structure that differs from the rest of the domain (Ricketts et al., 2023b). The choice of boundary condition that is applied changes the response in the near-boundary region, allowing it to be used to effectively reduce the spurious values that are introduced. Whilst the well-known Dirichlet and Neumann conditions can be specified, here the approach of Ricketts et al., (2023b) is taken, supplying a weighted Dirichlet-Neumann boundary condition

$$\left(\alpha X + (1 - \alpha) l \frac{\partial X}{\partial \mathbf{n}} \right) = 0 \quad \text{on} \quad \partial\Omega \tag{15}$$

where $\alpha \in [0, 1]$ is the weighting parameter which controls the ratio of the Dirichlet and Neumann components, noting that this is equivalent to the standard Robin condition

$$\left(\mathbf{X} + \lambda \frac{\partial \mathbf{X}}{\partial \mathbf{n}} \right) \Big|_{\partial\Omega} = 0 \tag{16}$$

where the Robin coefficient λ can be formulated from Eq. (15) as

$$\lambda = \lambda(\alpha, l) = \frac{1 - \alpha}{\alpha} l \tag{17}$$

Rather than assigning λ to be a standard value (Roininen et al., 2014), the weighted approach allows for further flexibility and tuning of the condition such that boundary effects can be minimised and an extended mesh for field generation is not required. For more details, see Ricketts et al., (2023b).

To solve the problem numerically, a finite element approximation is employed, such that

$$\mathbf{X} \approx \sum_{j=1}^N X_j N_j \tag{18}$$

where N_j are again the basis functions in $H^1(\Omega)$ and X_j is a vector of random variables. By applying Green's first identity and following the usual Galerkin choice, the problem is approximated as

$$\text{find} \quad \mathbf{X} \approx \sum_{j=1}^N X_j N_j \quad \text{such that} \quad b(\mathbf{X}, N_i) = \left\langle \mathbf{W}, \sqrt{\alpha l^d} N_i \right\rangle \quad \text{for all} \quad i = 1, \cdots, N_{dof}, \tag{19}$$

where b is a bilinear functional defined as

$$b(\varphi, \phi) = \int_\Omega \varphi \phi \mathrm{d}x + l^2 \int_\Omega \nabla \varphi \bullet \nabla \phi \mathrm{d}x + \frac{l^2}{\lambda} \int_\varsigma \varphi \phi \mathrm{d}\varsigma, \quad \varphi, \phi \in H^1(\Omega) \tag{20}$$

where $\varsigma = \partial\Omega$. Hence, the equivalent matrix equation is defined as

$$\left(\mathbf{M} + l^2 \mathbf{S} + l^2/\lambda \mathbf{B}\right) \mathbf{X} = \mathbf{W}, \tag{21}$$

where the solution $\mathbf{X}$ is a Gaussian random field, and the matrices $\mathbf{M}$, $\mathbf{S}$, $\mathbf{B}$, and the vector $\mathbf{W}$ are given as

$$M_{i,j} = \int_{\Omega} \psi_j \psi_i \mathrm{d}x, S_{i,j} = \int_{\Omega} \nabla\psi_j \bullet \nabla\psi_i \mathrm{d}x, B_{i,j} = \int_{\zeta} \psi_j \psi_i \mathrm{d}\zeta, W_i = \left\langle W, \sqrt{\alpha l^d}\psi_i \right\rangle \tag{22}$$

This process can also be carried out for both Dirichlet and Neumann conditions, leading to similar expressions (Ricketts et al., 2023b). As the generated field is merely a solution of the SPDE in $\mathbb{R}^2$, it can be assigned to represent any model parameter which is spatially varying within the model.

3. Numerical considerations

In this section, the components necessary for WR soils to be represented are given.

3.1. Constitutive model for hydrophobicity

For wettable soils, the van Genuchten model is often adopted to represent the saturation–capillary pressure relation, defined as

$$S_l = \left(1 + \left(\alpha_{vg} u_l\right)^{n_{vg}}\right)^{\frac{1-n_{vg}}{n_{vg}}} \tag{23}$$

where α_{vg} and n_{vg} are the van Genuchten parameters.

Whilst this is suitable for wettable unsaturated soil, it is not readily applicable to represent hydrophobic soil as it cannot model negative suctions. If a soil is wettable, then the water entry pressure (WEP) is overcome at positive suctions, but for WR soil, water entry can occur at negative suctions. Physically, this relates to positive pore-water pressures which are required to overcome the WEP and allow infiltration. This can be seen in Fig. 1 (after Zheng et al., (2021)), where conceptual illustrations of soil water retention curves for fine and coarse grained soils, as well as WR soils, are shown. The van Genuchten relation cannot account for the positive pore-water pressures that are characteristic of the mixed/strongly hydrophobic material soil, suggesting that an alternative relation for the soil water retention curve (SWRC) of these non-wettable layers is required.

Recently, Foroughi et al., (2022) proposed a new saturation–capillary pressure relationship for porous media of varying wettability, which proved to be more flexible and accurate than existing relationships. The relationship matched well against a wide range of experimental data, measured from rocks, soil, bead and sand packs, and manufactured fibrous materials. This approach is adopted here for media with mixed wettability. The relationship is as follows

$$S_l = \left(\frac{1}{\pi}\left(\frac{\pi}{2} - \tan^{-1}\left(\frac{s-A}{B}\right)\right)\right)^{\frac{1}{C}} \tag{24}$$

where A is an indicator of wettability, B is the curvature index, and C is the saturation exponent. Whilst there is no fundamental basis for its functional form, the given parameters of the function can be interpreted physically. The most important in this study is A, where $A > 0$ indicates a wettable or hydrophilic medium, $A < 0$ indicates hydrophobicity, and $A \approx 0$ suggests a mixed-wettable medium where locally the medium could be hydrophobic or hydrophilic. A also controls the water entry pressure. Similarly, B is the curvature index, quantifying the magnitude of capillary pressure, and C is the saturation exponent controlling the inflection point of capillary pressure. To the authors knowledge, these coefficients have not been directly related back to physical characteristic of porous media quantitatively, but are influenced by pore-structure and wettability (Foroughi et al., 2022). See Foroughi et al., (2022) for a visualisation of how changing each parameter affects the overall shape of the curve.

3.2. Random field application

Following the approach of Ricketts et al., (2023a), random fields are applied to represent material heterogeneity, these being generated and scaled such that they are representative of the desired material property. A key difference in this study is that the domain is considered as a layered continuum, where layers can be defined by variable material properties. In this study, we also consider water repellency, enabling consideration of a variably water repellent top layer and an underlying wettable sublayer.

In wettable layers, the generated Gaussian random fields are chosen to directly represent the saturated conductivity K_s, and the van Genuchten parameters α_{vg} and n_{vg}, leading to spatial variation in the SWRC and conductivity relations amongst other constitutive components.

However, for the hydrophobic layer, Foroughi et al.'s, (2022) relationship is adopted and spatial variation in the water retention function is accounted for by varying the parameters of equation (24), namely A, B, and C, throughout the layer. Along with these parameters, K_s is also varied (as in the wettable layers), which allows the unsaturated conductivity to vary spatially throughout the full domain. The relative coefficient of unsaturated hydraulic conductivity K_r for the WR layer is calculated as

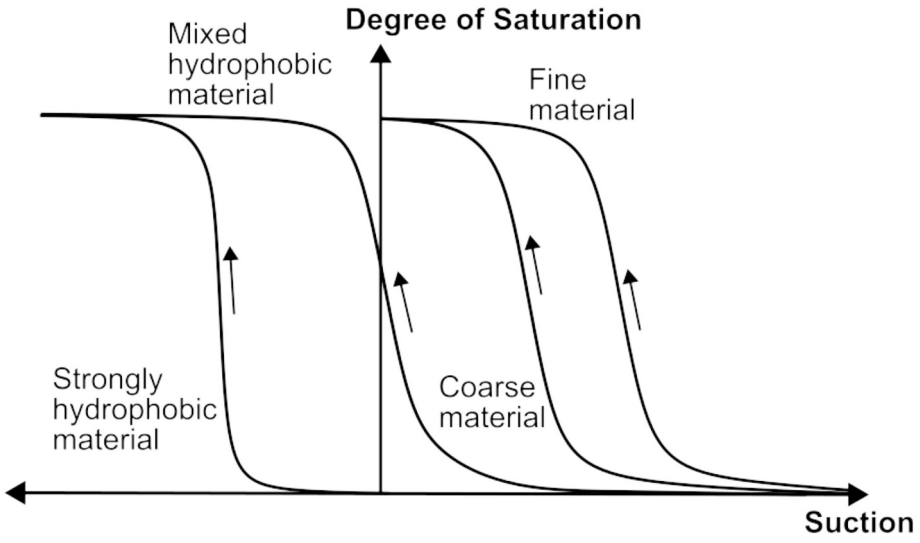

Fig. 1. Illustrative example of the soil water retention curves resulting from soils with differing levels of wettability (adapted from Zheng et al. (2021)).

$$K_r = \sqrt{S_l}\left[1 - \left(1 - S_l^{\frac{1}{m_{vg}}}\right)^{m_{vg}}\right]^2 \tag{25}$$

where $m_{vg} = 1 - 1/n_{vg}$ (Mualem, 1976). In WR layers, n_{vg} is parameterised using the particle size terms d_{60} and d_{10}, the grain sizes for which 60 % and 10 % are finer respectively, such that

$$n_{vg} = \frac{C_1}{\log_{10} C_u} + 1 \tag{26}$$

where C_1 is a model constant suggested as 1.07, and C_u is the coefficient of uniformity (Wang et al., 2019), defined as

$$C_u = \frac{d_{60}}{d_{10}} \tag{27}$$

Thus, in addition to K_s, A, B, and C, the terms d_{60} and d_{10} are varied spatially in non-wettable layers.

The model has been built such that an arbitrary number of random fields can be generated with differing correlation structures for various material properties. Here, the correlation structure of the particle size data is assumed to follow that of K_s, meaning that larger particle sizes relate to more conductive regions, where the contrary is also true.

It should be noted that when using equation (24), the concept of relative permeability in its traditional sense does not apply to WR soils due to their fundamentally different wetting behaviour. The hydraulic conductivity in WR regions is controlled by the measured K_s values and the water entry pressure through the constitutive relationships, rather than through a modified relative permeability function. This approach maintains consistency with experimental observations whilst avoiding the need to develop new relative permeability models for hydrophobic conditions, which is out of scope of the current study.

3.3. Transition region

When modelling layered materials, the interface between layers is often assumed to be discrete, such that there is no mixed-material transition zone (Romano et al., 1998; Liu et al., 2015; Ahmadi et al., 2016). In many cases, it is not representative of the problem to have such idealised interfaces (Heilig et al., 2003). This is especially true when the layers represent variation in the same basic material type, such as different levels of repellency per layer. For naturally induced WR, be it through wildfire or contamination, the level of repellency is generally very high near the surface and decaying with depth (Woods et al., 2007). One approach to represent this is to assume a localised mixture of wettable and WR media within a representative elementary volume, with the ratio of each fraction varying with depth. As the model considers discrete water retention functions in each layer, by interpolating between them based on the depth in a predefined transition zone, a combined water retention function can be calculated. This is based on the assumption that the ratios of each fraction within a transition layer varies with depth. Similarly, other material parameters that are shared between layers can vary in the same way, such as K_s. A similar approach was taken in Dou et al., (2021), where a transition layer was implemented with linear variation in K_s normal to the layer interface. Here, this is taken further, allowing for variation in multiple material properties simultaneously with correlated random fields, providing a more comprehensive representation of the heterogeneous nature of real soil systems.

To illustrate this, we consider the top 20 cm layer of the domain detailed in Section 4. This comprises a 5 cm top layer that is assumed water repellent, and transitions over 15 cm to being fully wettable. Further justification for this is given in Section 4, whilst the focus here is on the numerical details. A transition zone of 15 cm is assumed, starting at 5 cm depth, and ending at 20 cm depth. To implement this computationally two random fields f_1, f_2 are generated for the full domain and are scaled based on the desired material properties of each layer. The interpolated field is then calculated as

$$f_I = (1 - \vartheta) f_1 + \vartheta f_2 \tag{28}$$

ϑ is the following sigmoid function

$$\vartheta = \frac{1}{1 + e^{\omega \epsilon(x)}} \tag{29}$$

where ω is a smoothness coefficient of the sigmoid function, and the function ϵ varies with the depth x, according to equation (30). By varying the value of ω, the smoothness of the sigmoid function can be changed, such that sharp or slow transitions between f_1 and f_2 can be achieved. The sigmoid function is chosen to allow a smooth transition between layers, this assumption is addressed at the end of this section. Equation (29) is dependent on ϵ, and is calculated using a simple linear interpolation based on the beginning and end of the transition zone as

$$\epsilon(x) = \frac{(x - x_{\text{tmin}})(\epsilon_{\max} - \epsilon_{\min})}{x_{\text{tmax}} - x_{\text{tmin}}} + \epsilon_{\min} \tag{30}$$

where $\epsilon_{\max}$, $\epsilon_{\min}$ define the arbitrary range of the sigmoid function which is used for interpolation. Here, $\omega = 0.2$ and $\epsilon_{\max}$, $\epsilon_{\min}$ are defined as 10 and -10 respectively. The parameters $\epsilon_{\max}$ and $\epsilon_{\min}$ are arbitrary scaling bounds, serving only to provide numerical stability during the transition between WR and wettable states. The physically meaningful parameter controlling this transition is ω, which determines the width of the zone over which the interpolation occurs. In reality, depending on the soil type and characteristics, this region could be much smaller physically when considering transitions more typical wettable soils (Heilig et al., 2003).

Whilst the example above is illustrative for arbitrary fields f_1 and f_2, the same procedure is carried out for interpolation between the SWRCs of adjacent layers and is demonstrated in the following section. Through this method, the transition region and its smoothness can be defined in an intuitive manner, such that the transition between layers with depth follows the path of a sigmoid function.

4. Application: field infiltration experiment

4.1. Experimental details of Lipsius and Mooney (2006)

The field experiments carried out by Lipsius & Mooney (2006) are considered, where field infiltration experiments were conducted to investigate the influence of water repellency on infiltration patterns. The soil considered was contaminated with heavy metals (Chromium and Arsenic) due to the leaching of wood preservatives from impregnated wood located at an industrial site in Bavaria, Germany. Similarly, it was also observed that polycyclic aromatic hydrocarbons had entered the topsoil from tar-oils (Hopp et al., 2006). Both resulted in alterations in the chemical and physical properties of the soil, inducing strong water repellency and the prevention of plant growth. The measured soil physical properties, including bulk density, particle size data, and the saturated conductivity (measured within saturated columns using a constant head apparatus), are given in Table 1.

In both the spring and summer, dye tracer infiltration experiments were conducted such that the effects of seasonal variability could be quantified. The 2 m^2 plots were selected because their flat, vegetation-free surfaces were expected to exhibit higher contamination levels. Brilliant Blue FCF (C.I. 42090) of concentration 2 g L^{-1} was irrigated manually on two plots –using a watering can- with different irrigation rates applied to each: (i) 10 mm/h for 2.5 h, and (ii) 14.3 mm/h for 3.5 h. The rate of application varied due to ponding and surface runoff. A day later, the plots were excavated to a depth of 1 m and the profiles were photographed for later analysis. Ten profiles were sampled in roughly 40 cm intervals for each plot. As the seasonal variability was found to be negligible between the spring and summer (Lipsius and Mooney, 2006), the following analysis considers the case of 10 mm/hr

Table 1
Soil properties of the experimental site, where n_O is the number of observations (Lipsius and Mooney, 2006).

			Particle size data					
Depth (cm)	n_O	Bulk density (g cmˆ-3)	>2mm (%)	630μ m-2 mm (%)	200-630μ m (%)	63-200μ m (%)	<63μ m (%)	K_s(cm dˆ-1)
1–10	18	1.51	0.4	40.6	48.6	9.9	0.6	500
10–19	20	1.56	0.5	37.4	53.5	8.1	0.4	664
19–22	4	1.55	0.7	30.9	58.7	8.9	0.5	745
22–50	1	1.71	0.2	26.2	62.6	10.6	0.4	2500
>50	20	1.6	0.1	23.5	65.5	10.7	0.4	850

irrigation rate in the summer period.

4.2. Numerical details

As stated in the previous section, random fields are employed to represent variations in K_s, A, B, C, α_{vg}, n_{vg}, d_{60}, and d_{10}, where the variability of the given parameters propagate throughout the relations used in calculating the constitutive components of the model. The mean and standard deviations of the given parameters are based on the experimental data reported in Lipsius & Mooney (2006) where available, with additional parameters for the hydrophobic constitutive model (A, B, C) assumed based on typical values for WR soils reported in Foroughi et al. (2022) (see Table 2).

Volumetric water content data from both stained and unstained soil regions provided the experimental basis for parameter estimation (Lipsius & Mooney, 2006). The underlying assumption that WR soil leads to unstained regions, as infiltration and subsequent staining would otherwise occur, led to estimation of the water entry pressure (WEP) within the upper 20 cm soil layer. Parameter A was calibrated such that its mean value positioned the inflection point at the average WEP, whilst its standard deviation captured the observed WEP variability (ranging from approximately 230 Pa to 9025 Pa). Following Foroughi et al., (2022), who demonstrated parameter C typically assumes unity for mixed wettability media, the mean value of C was set to 1. Parameter B was selected to ensure curve smoothness consistent with the wettable region behaviour. The standard deviations of parameters B and C, which have considerably less influence on model response than parameter A, were determined through sensitivity-based tuning.

To avoid non-physical scaling of the fields, the assumed normal distributions of the parameters are capped at 3 standard deviations from the mean. As the correlated structure of the soil was not given, l was assumed to be 0.2 m vertically, and 0.1 m in both horizontal directions to account for local variations in material properties. These correlation lengths were selected to reflect site-specific structure in the contaminated sandy soil used for model calibration. Lipsius & Mooney (2006) showed that water repellency is confined to the topsoil, declines rapidly with depth, and that a sharp decrease in stained area and a change in flow behaviour occur around 20 cm. As such, the vertical correlation length was set to 0.20 m to span the depth over which repellency decays and the horizon transition organises flow. Laterally, dye-coverage statistics and image analysis at 5 cm resolution revealed small-scale patchiness and high variability in vertical cross-sections (Lipsius & Mooney, 2006). As the identified fingers had lateral scales on the order of 10 cm, a shorter horizontal correlation length of 0.10 m was chosen to represent these smaller infiltration patches and avoid over-smoothing lateral heterogeneity, consistent with the observed flow heterogeneity and finger organisation.

The most influential spatially varying parameter for the WR layer is A, as this largely controls the WEP and the level of water repellency that a given position in the domain has. Larger variations in A across the domain will lead to more unstable flow, with more strongly pronounced fingering behaviour. It also allows for positive pore-water pressures to be assigned as WEPs, as suggested by Fig. 1.

The simulation domain is defined as a 1 m cube, discretised by regular hexahedral elements of element length 2 cm (with appropriate convergence checks undertaken), and can be seen in Fig. 2 (a) along with the applied boundary conditions. A rainfall flux boundary condition was applied using a variable application method (Ricketts et al., 2024). This is where the applied flux is distributed across the boundary based on the material heterogeneity present at the surface, depending on K_s, leading to more conductive regions receiving more mass than less conductive regions. The remaining boundaries are assumed zero flux. An initial timestep of 10 s was used, which was then increased to 100 s when the wetting front became less sharp, leading to convergent results. The total simulation time was 27.5 h as experimentally, the tracer was applied for 3.5 h, with the soil being imaged an assumed 24 h later. The layered configuration of the soil is seen in Fig. 2 (b), where the transition zone spans 15 cm of the domain, annotated in red.

The top part of the soil is assumed fully hydrophobic, and the bottom section assumed wettable. The size of the water repellent and transition layers were based on detailed analysis of the experimental plots in Lipsius and Mooney (2006). Water drop penetration tests (WDPT) revealed that the upper 1–8 cm exhibited severe water repellency, which progressively decreased until approximately 18 cm depth, with no repellency observed beyond 20 cm. Based on this profile, the model domain comprised a 5 cm purely WR upper layer followed by a 15 cm transition zone. Sensitivity analysis demonstrated that extending the purely WR region from 5 to 8 cm produced negligible changes in the simulated infiltration patterns, supporting the selected parameterisation. This configuration appropriately captures the substantial variability in surface water repellency (WDPT: 7440 $\pm$ 5400 s) whilst reflecting the observed gradual reduction in repellency with depth.

Heterogeneity in the level of WR is due to the way that solutes would have infiltrated the soil over time, permeating in a non-uniform manner. As they move preferentially through the soil, this renders certain regions more WR than others, with the overall level decreasing from the surface with depth. By assuming a sigmoidal variation with depth in the fractions of wettable and WR soil at any particular location, as in Section 3.3, the variation in WR with depth is represented. Similarly, coupling this with the random fields for local spatial variations in the hydraulic behaviour allows for the heterogeneity of both the material and level of hydrophobicity to be represented. Fig. 3 gives example fields of the

Table 2
Random field mean and standard deviation values.

		K_s[m/s]	α_{vG}[Pa^{-1}]	n_{vG}	d_{60}[mm]	d_{10}[mm]	A	B	C
WR	*Mean*	6.74E-05	–	–	0.3471	0.1215	−50	500	1
	Standard Deviation	1.34E-05	–	–	0.0062	0.0008	750	3	0.05
Wettable	*Mean*	1.58E-04	4.513E-04	3.2278	–	–	–	–	–
	Standard Deviation	5E-05	7.00E-05	0.0732	–	–	–	–	–

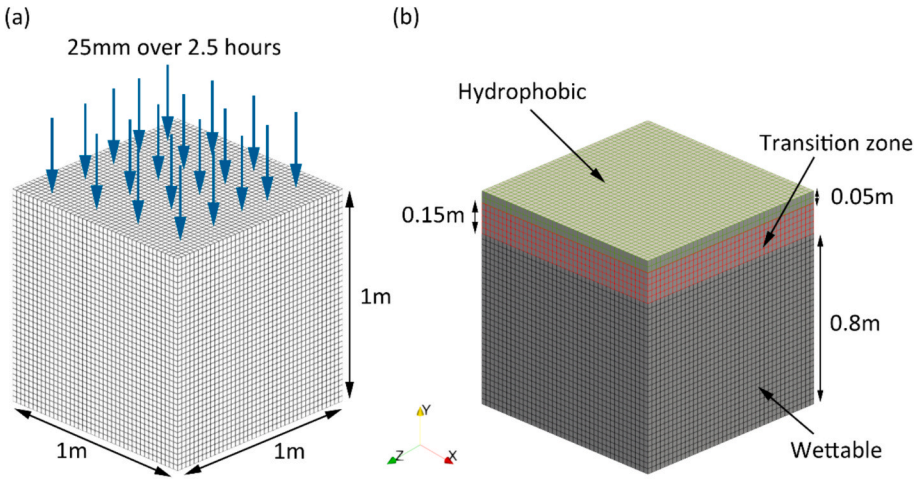

Fig. 2. Numerical domains showing (a) the mesh and applied boundary conditions, and (b) the size and type of soil layers.

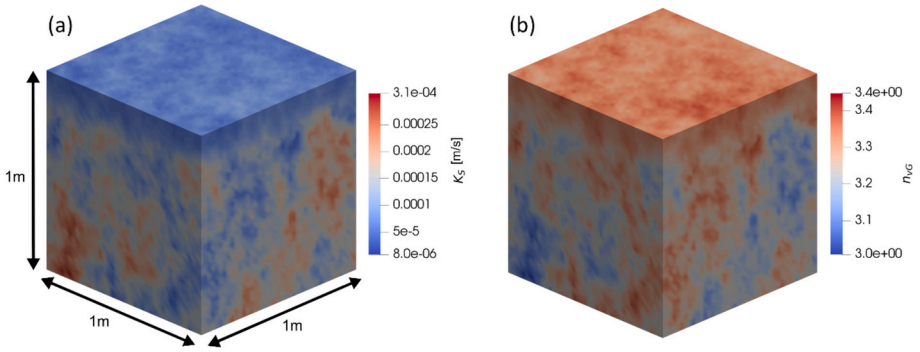

Fig. 3. Random field realisations to highlight the transitional behaviour for (a) K_s and (b) n_{vg}.

numerical domain based on the values given in Table 2 for K_s and n_{vg}, where the variations in the mean values reflect the changing properties in the transition zone between layers.

As mentioned above, the SWRC for the transition region is calculated as an interpolation between the respective layers' constitutive relation. At a depth of 0.05 m, the WR relationship is used to compute the degree of saturation, as highlighted in Fig. 4 (a). As the depth increases through the transition zone to 0.2 m, the curve is interpolated, finally being fully wettable from 0.2 m onwards. The curves presented in Fig. 4 (a) are the interpolated SWRCs based on the mean values given in Table 1, where in the model, the presented curves for a given depth will strongly vary as in Fig. 4 (b) (for a depth of 0.0125 m). In Fig. 4 (b), curves were plotted based on the full variation of parameters given in Table 1 to show the banding of the SWRC that is present in the model for a specific depth in the transition zone. It is seen that the WR section exhibits more variability compared to the wettable section.

4.3. *Tracer simulation results*

Three representative simulations R1, R2, and R3 are presented from

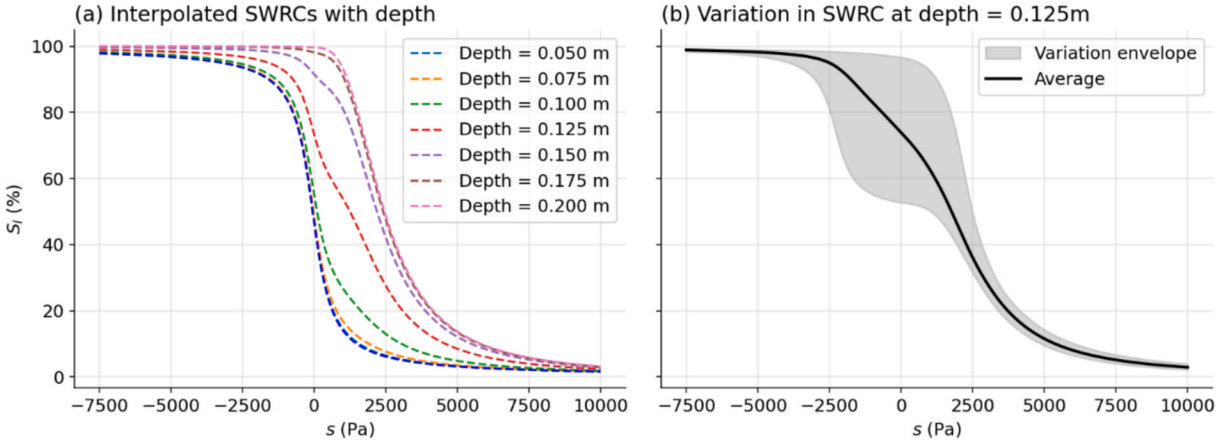

Fig. 4. Illustration of (a) Average interpolated SWRCs between the wettable and water repellent soil, where the red dashed line at a depth of 0.125 m is the middle of the transition zone; and (b) the variation in the interpolated SWRC at depth of 0.125 m.

a set of 20 analyses. These are illustrative of the full behaviour that the model can represent, and are quantified in Section 4.4 based on the simulated dye coverage. For further results from the simulations conducted, see Appendix B. Fig. 5 shows the fields of K_s for R1, R2, and R3 respectively, highlighting the local and global variation in K_s across the two layers and their transition zone.

Fig. 6 shows the wetting front movement at 1000, 6000, 10,000, and 98,000 s for R2, where both R1 and R3 had similar responses.

As described above, a tracer applied to the surface allowed for imaging of the infiltration profiles. The 35 % degree of saturation threshold is consistent with Lipsius and Mooney's observations of the mean moisture contents in stained and unstained areas.

Fig. 7 shows the tracer activation regions for R1, R2, and R3 at the final timestep of 27.5 h, where the top row of images shows this in blue. The bottom row shows this same area as a translucent layer to visualise the non-uniform nature of the tracer regions.

Finally, slices were taken from the three presented simulations to compare with the experimental images based on the dye coverage percentage and the spatial distribution of the fingered shapes. These can be seen in Fig. 8, where (a), (b), and (c) are the experimental images, and (d), (e), and (f) are the numerical slices taken from R1, R2, and R3 respectively. The specific slices that are presented were chosen based on their ability to match well with the limited experimental data, whilst also being representative of the overall model response. Further slices can be seen in Appendix B, highlighting the range of flow characteristics that can be represented. The percentage of dye coverage can be used to compare the results of the numerical simulations against the experimental observations, indicating the ability of the model to represent the overall wetting front response.

A sensitivity analysis was also conducted to establish the variation in results based on changes in critical material properties which were largely inferred from the available data in Lipsius and Mooney (2006). The parameters assessed were the vertical and lateral correlation lengths, A, B, C of Equation (24), and ω of Equation (29), the results of these analyses are found in Appendix A. This was undertaken using case R2, reported in Section 4, as the reference case (using the same random seed). Varying the correlation lengths between 0.1 m horizontally and 0.2 m vertically, and 0.1 m horizontally and 0.1 m vertically, showed little variation in the fingering characteristics (see Fig. A1), being quantified through dye coverage similarly to Fig. 8. The mean values of A, B, C were varied by ± 3 standard deviations as in Table 2, where variations in B and C saw almost no change in the tracer profile characteristics (see Figs. A3 and A4). The largest variation was seen through changing A which controls the level of wettability of the top layer and its WEP (Fig. A1), and ω which changes the range over which the top and bottom layers transition (Fig. A5). Decreasing the mean value of A to a larger negative pore water pressure led to marginally larger fingers being formed, where increasing the mean value led to the water passing more quickly through the top layer as it is more hydrophilic, reducing the build up of tracer in the layer. Finally, varying ω from 0.1 to 0.5, where smaller values result in a larger transition zone, indicated that above values of $\omega = 0.2$, the value chosen for this study, further increasing the parameter shows minimal change in fingering characteristics which are representative of the experimental observations of Lipsius and Mooney (2006). Lower values of ω (resulting in a relatively large transition zone) resulted in deeper dye penetration and less pronounced fingering.

It is clear that the range of responses seen in Fig. 8 (a-c) are well represented by the numerical results Fig. 8 (d-f). This is in terms of the spatial distribution of tracer activation and dye coverage percentages. One aspect that does not compare well is the large dye coverage in the first bar of the horizontal projection of Fig. 8 (d-f), relating to tracer activation in the surface elements. This is a result of fluid infiltration at the surface being represented by a flux boundary condition. In reality, and as stated in the original experimental study, water will infiltrate at a variable rate, where both runoff and ponding were observed. In this way, water would infiltrate at a pace directly dictated by the material properties, as opposed to the numerical scheme. On the other hand, the dye coverage of the later regions is well within the experimental range, showing an adequate match with the test data. Importantly, the model exhibits wetting front patterns that have the similar characteristics as those observed in the experiments. This could allow for uncertainty in experimental readings to be considered, rather than assuming there is no associated error.

As in Ricketts et al., (2023a), it is observed that in the wettable layer, less conductive regions see a larger build-up of water, suggesting the increased chance that the tracer will be active in such a region. Conversely, the more conductive regions allow for faster passage of the wetting front, taking the tracer with it. Similarly, Fig. 6 (b) illustrates the change in hydraulic response through the domain as the transition region is reached. The flow becomes more diffuse due to the smaller variation in the SWRC for the wettable regions. This is in agreement with the assumed behaviour of the medium, such that the water repellency should induce highly unstable flow that becomes more stable as it transitions into the wettable layer.

Due to the water repellency in the top layer, there is a period of time in the simulation for which the pore water pressure builds up at the surface. This lasts until the WEP is achieved for a given position, after which the water enters the soil body in a preferential manner. This can be seen in Fig. 9, where (a) shows the build-up of fluid at the surface illustrated by a higher degree of saturation, (b) shows a time after the WEP has been surpassed, and (c) gives a point further into the simulation

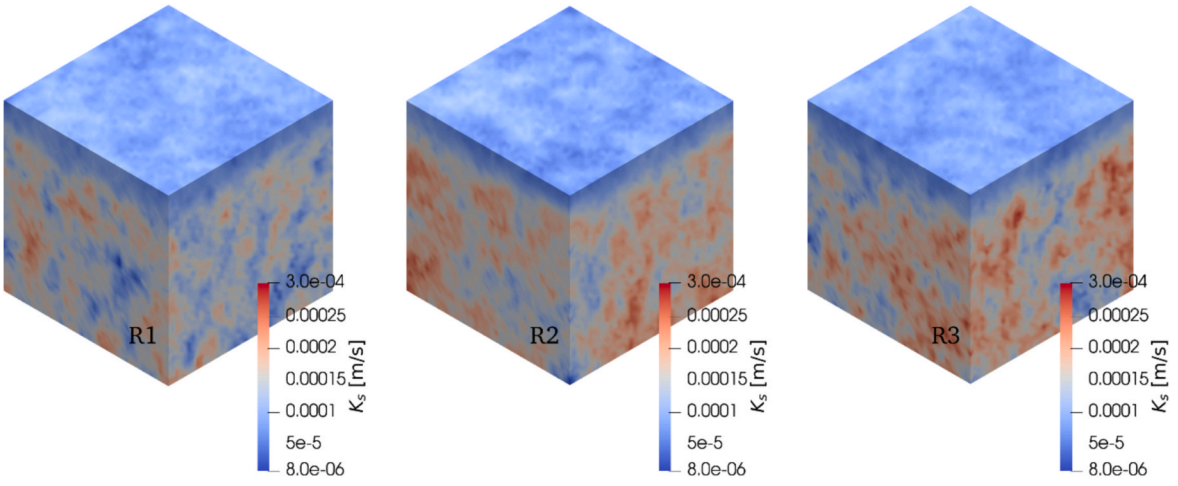

Fig. 5. Generated random fields of K_s.

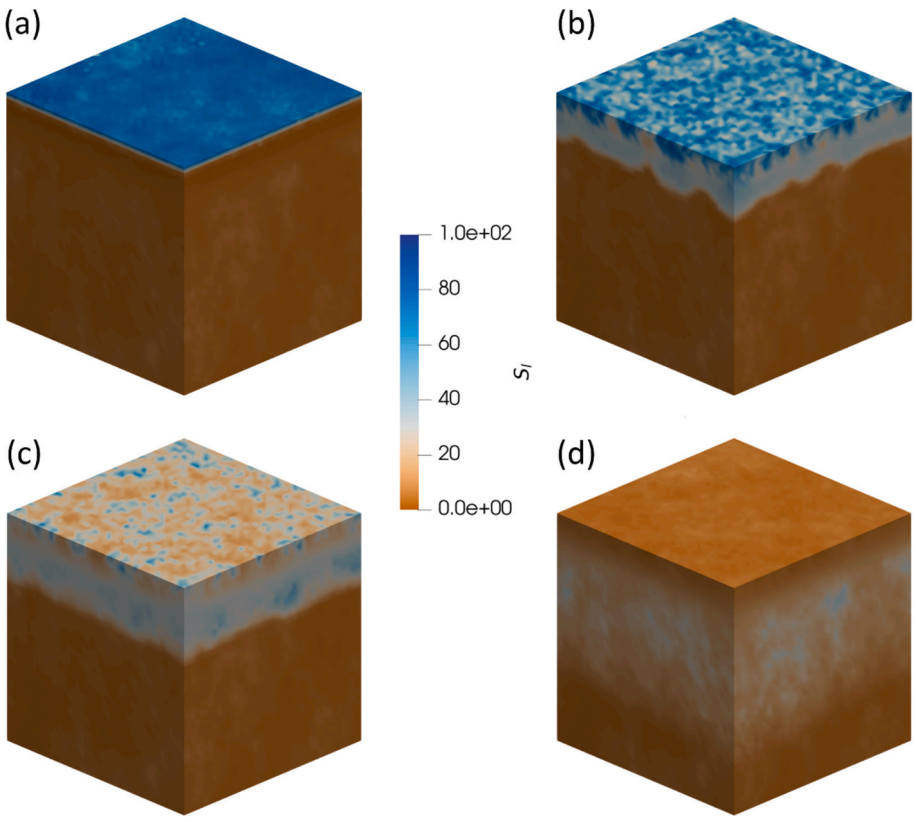

Fig. 6. Wetting front movement in terms of the degree of saturation S_l of R2 at (a) 1000, (b) 6000, (c) 10000, and (d) 98,000 s.

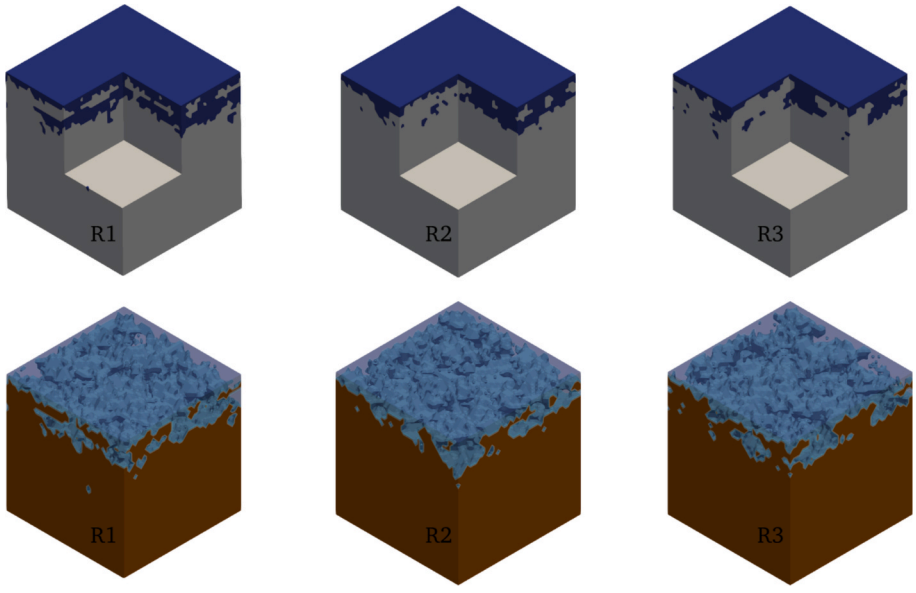

Fig. 7. Tracer activation regions at 35% S_l for R1, R2, and R3, where the top row shows the tracer in blue, and the bottom shows the same as a translucent layer to highlight the lateral variation.

to show the water passing through the hydrophobic layer in a fingered fashion.

The results given in (a-c) are at times 16 min, 33 min, and 1 h respectively. At 1 h, the average depth of the water level was 7.2 cm. It is clear that in (a), the degree of saturation −and therefore porewater pressure- is much higher than that of the later plots. As the WEP is dependent on the SWRC at the given position on the surface, which vary based on the material variability, the water begins the infiltrate at different times causing highly unstable behaviour. The flux is still being applied in (a-c), showing that once the WEP has been surpassed, the applied fluid will infiltrate into the soil body with less resistance and less build up at the surface.

To further illustrate the unstable flow patterns that result from the material variability, the flux of the invading fluid was computed for slices within the wetting front (see Appendix C). The fully 3-D nature of the flow is observed, where strong lateral fluxes are highly influential

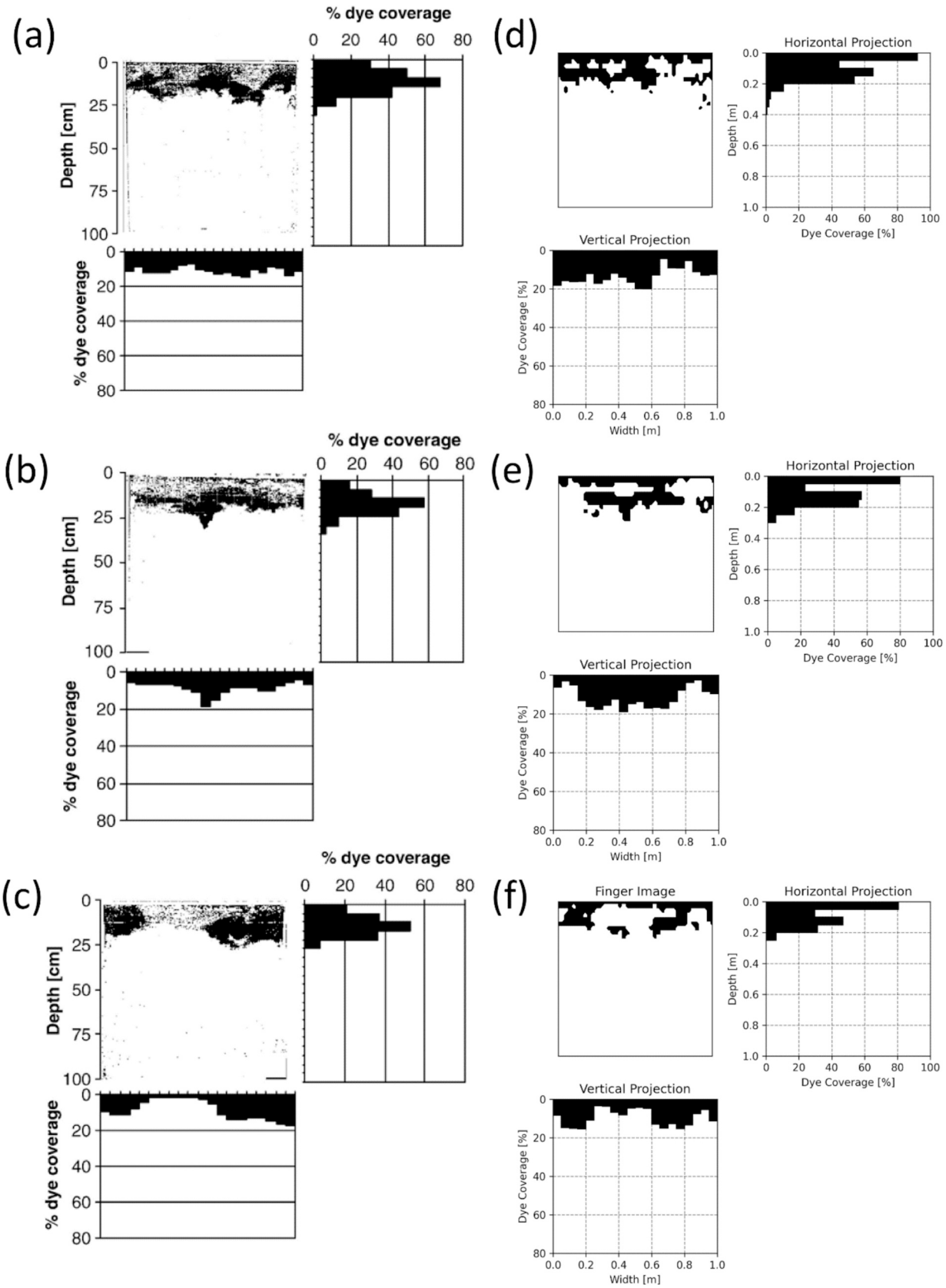

Fig. 8. Tracer activation regions and their respective dye coverages for vertical and horizonal projections, where: (a-c) are the experimental observations (after Lipsius and Mooney (2006)), and (d-f) are slices of R1, R2, and R3 respectively.

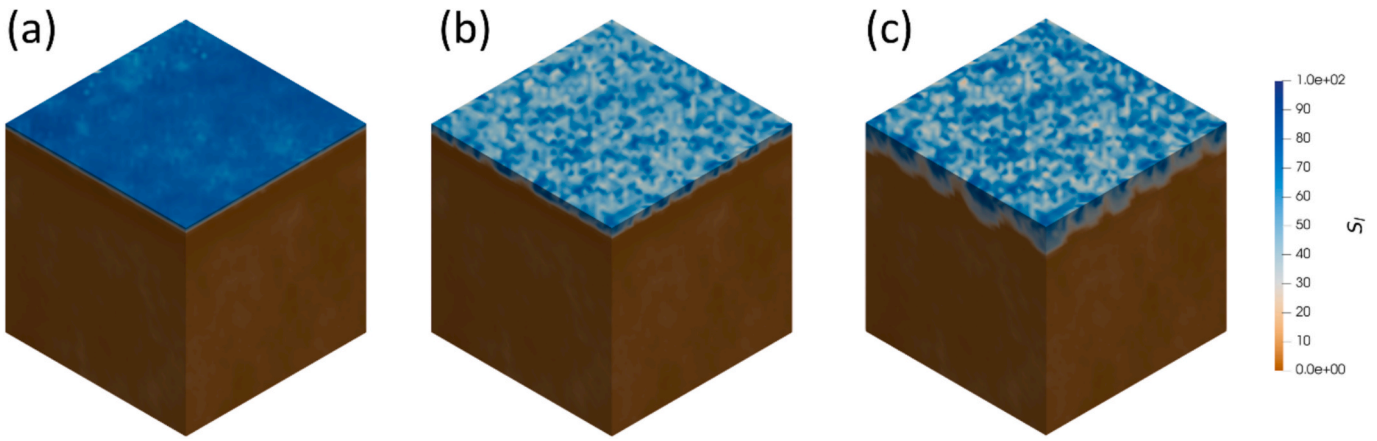

Fig. 9. Illustration of (a) a build-up of degree of saturation on the surface due to hydrophobicity at 16 min, (b) the fluid phase infiltrating after the pore water pressure has surpassed the water entry pressure at 33 min, and (c) a later stage to show the resulting fingered nature of the flow at 1 h.

over the movement of the fluid phase.

4.4. Uncertainty of dye coverage

To quantify how representative the presented simulations are in terms of the global behaviour of the model, the same approach as in Ricketts et al. (2023) has been employed. Here, the dye coverage is considered, being quantified in both the horizontal and vertical projections for direct comparison with the experimental data. In total, 20 simulations were conducted to assess the level of confidence. For each simulation, slices from each element layer in the x and z plane were taken of the solution such that the maximum, minimum and mean dye coverage could be determined. For a given simulation, this resulted in 80 slices due to the chosen element size. Once collected, the mean value of the maximum, minimum and mean dye coverage of all slices of a given simulation was taken. Finally, the confidence intervals were calculated over the mean of the maximum, minimum and mean dye coverage, resulting in 3 values of confidence and their respective ranges for each of the 20 sequential simulations.

The dye coverage reported in Lipsius & Mooney (2006) suggested that between 8 and 40 % of the domain was dyed. This is accounting for both 25 mm and 50 mm applied head, as well as both spring and summer results. The wide range of dye coverage results from both the 50 mm applied head tests and some individual spring measurements showing larger coverage values, though Lipsius & Mooney (2006) reported that the average seasonal differences were not significant. For the case of 25 mm in the summer period, as seen in Fig. 8 (a-c), these percentages are much lower.

Table 3 illustrates the mean, and upper and lower bounds for the maximum, minimum and mean dye coverage for both the horizontal and vertical projections calculated using data from all 20 simulations. It can be seen that the range of the values vary, but are small enough to show model consistency, suggesting that the response of the model is consistent whilst allowing for highly varied infiltration profiles. The percentage values given for the maximum dye coverage are typically larger than the experimental equivalent, but as suggested previously, this can be attributed to the numerical application of flux at the surface. Similarly, the percentage values match well with those given in the histograms of Fig. 8 (a-c). The confidence in the confidence intervals of the observed quantities is $\geq$ 99 % for the horizontal projection, and $\geq$ 99 % for the vertical projection.

Table 3
Calculated ranges of dye coverage based on all 20 simulations for the maximum, minimum and mean dye coverage in both horizontal and vertical projections.

Projection	Dye Coverage	Lower Bound (%)	Mean (%)	Upper Bound (%)
Horizontal	*Minimum*	2.34	2.94	3.98
	Mean	12.26	13.03	13.89
	Maximum	81.85	85.11	88.73
Vertical	*Minimum*	3.46	4.23	5.01
	Mean	12.26	13.03	13.89
	Maximum	20.10	21.58	22.79

The convergence of the confidence in the calculated intervals can be seen in Fig. 10. As the number of simulations increases, the confidence in the calculated interval converges to above 95 %, as seen in Fig. 10 (a). The evolution of the confidence intervals for a given level of confidence was also calculated, and is shown in Fig. 10 (b) where the convergence of the confidence intervals for an assumed confidence of 95 % is observed. Fig. 10 (a) and (b) relate to the horizontal dye coverage statistics, where the same observations and conclusions are seen for the vertical projection also (see Fig. 11). As is expected, there is more uncertainty in the vertical dye coverages due to the larger variations in the vertical histograms in Fig. 8 and the additional plots in Appendix B.

5. Conclusion

This paper describes the development and appraisal of a stochastic model for hydrophobic soils. The model successfully demonstrates that fingered flow patterns observed in water-repellent soils can be suitably reproduced through the integration of three key components: an alternative SWRC for water-repellent conditions, spatially correlated random fields, and a novel transition zone representation.

The first of these components is an alternative SWRC which allows for water entry pressures that are characteristic of water repellent soil. In this way, the pore water pressure can build up on the surface where the boundary condition is applied, mimicking the resistance to infiltration that WR soils exhibit. By using the alternative saturation–capillary pressure relation and spatially varying its parameters, the local variations lead to fingered vertical profiles which matched well with the experimental observations. Similarly, by assuming an averaged mixing of the adjacent layers in terms of their level of wettability with depth, a more realistic representation of the domain in transition regions in this area was achieved. Its implementation is highly flexible and allows for arbitrarily sized transition zones whose smoothness can also be defined.

A key finding is that the model achieved high levels of confidence with very few simulations. The dye coverage of the soil profiles was used to quantify the model response, and is seen to match well with the experimental observations. The use of confidence interval calculations to quantify the model response in terms of the dye coverage was seen to be suitable in determining convergence criteria for multi-simulation regimes. Critically, this approach required only 13 simulations to

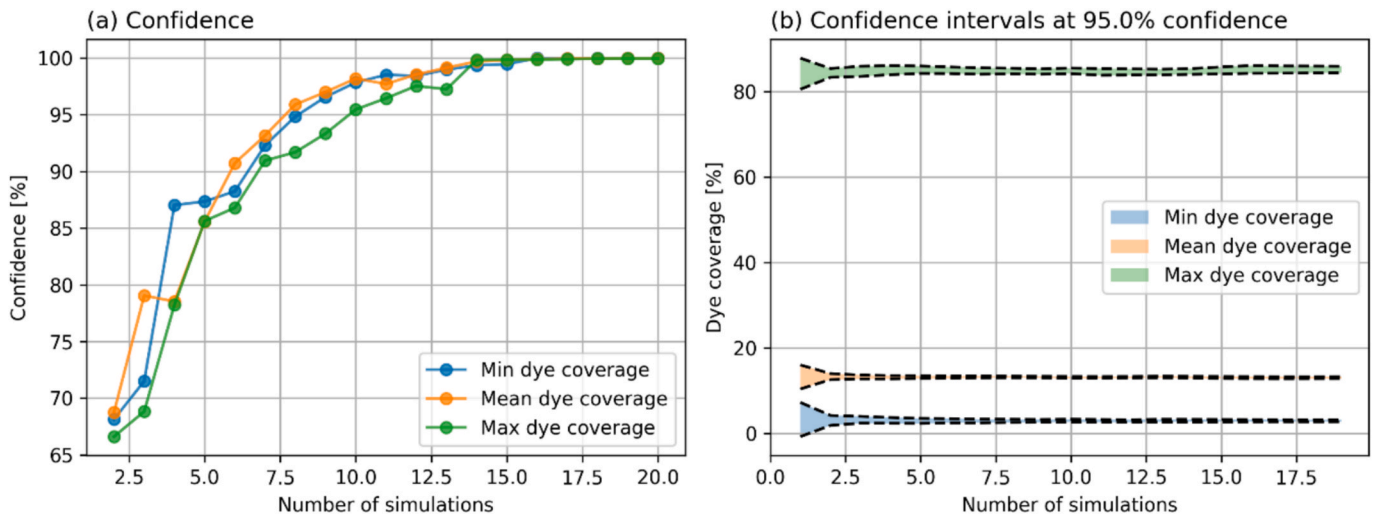

Fig. 10. (a) Confidence in the calculated intervals of the investigated parameters of dye coverage in the horizontal projection, and (b) the convergence of confidence intervals for dye characteristics at 95% confidence.

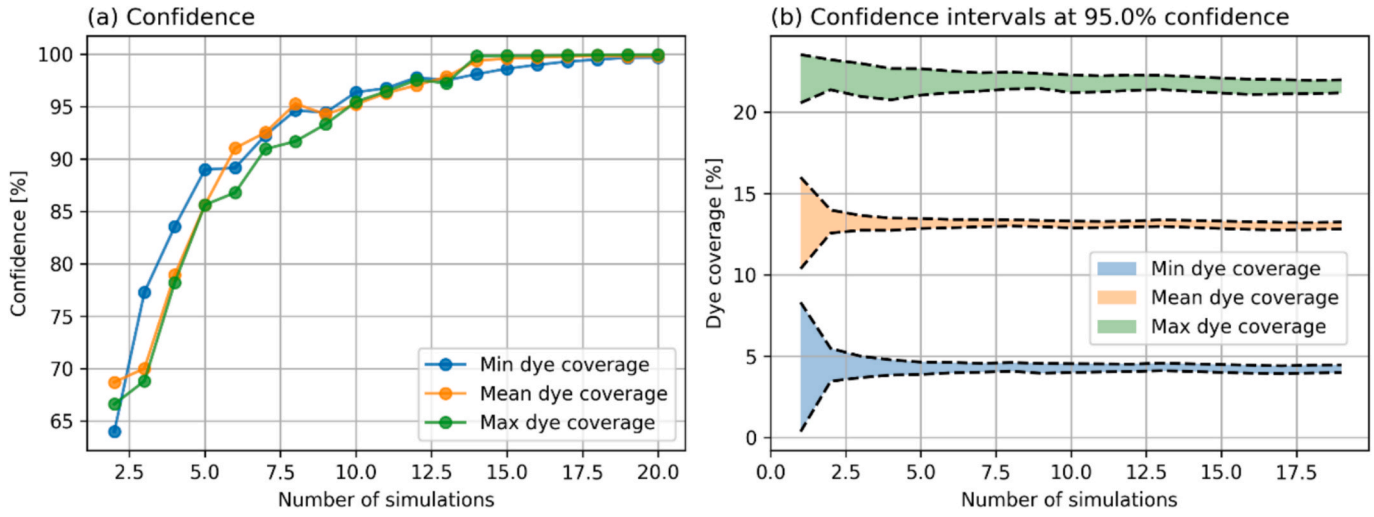

Fig. 11. (a) Confidence in the calculated intervals of the investigated parameters of dye coverage in the vertical projection, and (b) the convergence of confidence intervals for dye characteristics at 95% confidence.

achieve 95 % confidence intervals, orders of magnitude fewer than traditional Monte Carlo methods, demonstrating the efficiency of the stochastic framework. This allows one to run a very low number of simulations, whilst also ensuring that the results that have been obtained are representative of the population response of the model. With only 13 simulations, the population ranges of the maximum, minimum and mean dye coverages were calculated to 95 % confidence. Quantifying model responses in this way gives a good descriptor of the typical behaviour a model can portray, but is dependent on the indicators used for its quantification. Furthermore, the results definitively establish that 3-D analysis is essential for capturing the complex hydraulic behaviour of water-repellent soils. Strong lateral fluxes were observed throughout the domain, suggesting that a 1- or 2-D analysis would not capture the full effects and could lead to much more conservative hydraulic behaviour.

Whilst the results from Section 4 show a strong similarly to the experimental data, several limitations should be acknowledged. The representation of water repellency through the modified SWRC remains a simplification of complex physiochemical processes related to water repellency occurring at the pore scale. The model also assumes that the transition zone follows a smooth sigmoidal variation, which may not capture abrupt changes in wettability that can occur in some soils. Also, the parameters A, B, and C of the WR SWRC are inferred from experimental data rather than being related quantitatively with classical soil parameters. A sensitivity study showed that the A parameter, which controls the level of wettability of the top layer and its WEP and ω which changes the range over which the top and bottom layers transition (Fig. A5) had the most influence on the modelled results. However, the modelled behaviour, within the range of variation considered ($\pm 3\sigma$), remained realistic and close to the reported experimental results.

Despite these limitations, the model's ability to reproduce experimental infiltration patterns suggests that the chosen simplifications capture the essential physics of the problem whilst maintaining computational tractability.

CRediT authorship contribution statement

Evan John Ricketts: Writing – review & editing, Writing – original draft, Visualization, Validation, Software, Methodology, Investigation, Formal analysis, Data curation, Conceptualization. **Peter John Cleall:** Writing – review & editing, Supervision, Methodology, Conceptualization. **Anthony Jefferson:** Writing – review & editing, Supervision,

Methodology, Conceptualization. **Pierre Kerfriden:** Supervision. **Paul Lyons:** Supervision.

Declaration of competing interest

The authors declare that they have no known competing financial interests or personal relationships that could have appeared to influence the work reported in this paper.

Appendix A

The following contains results from a sensitivity analysis conducted for the vertical and lateral correlation lengths, A, B, C of Equation (24), and ω of Equation (29). The case is different from those presented in Section 4, but still showing fingering characteristics that are indicative of the soil investigated. All material properties, initial and boundary conditions follow from Section 4 except for the variation in named parameters and the random fields seed value.

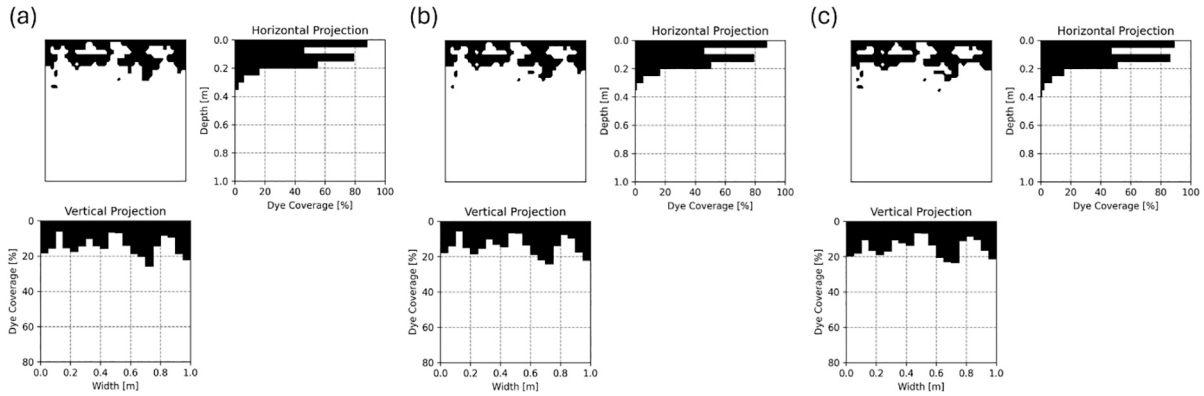

Fig. A1. Slices of the domain and their respective dye coverages to highlight the tracer activation region at 35 % degree of saturation when varying the correlation lengths as (a) 0.1 m horizontally and 0.2 m vertically (R2 reference value), (b) 0.1 m horizontally and 0.1 m vertically, and (c) 0.2 m horizontally and 0.1 m vertically,

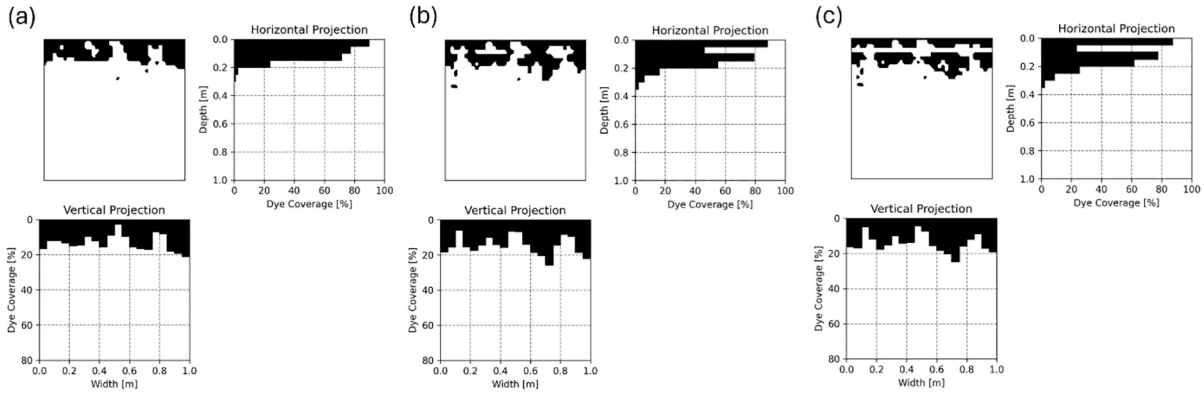

Fig. A2. Slices of the domain and their respective dye coverages to highlight the tracer activation region at 35 % degree of saturation when varying of Equation as (a) 2200, (b) −50 (R2 reference value), and (c) −2300

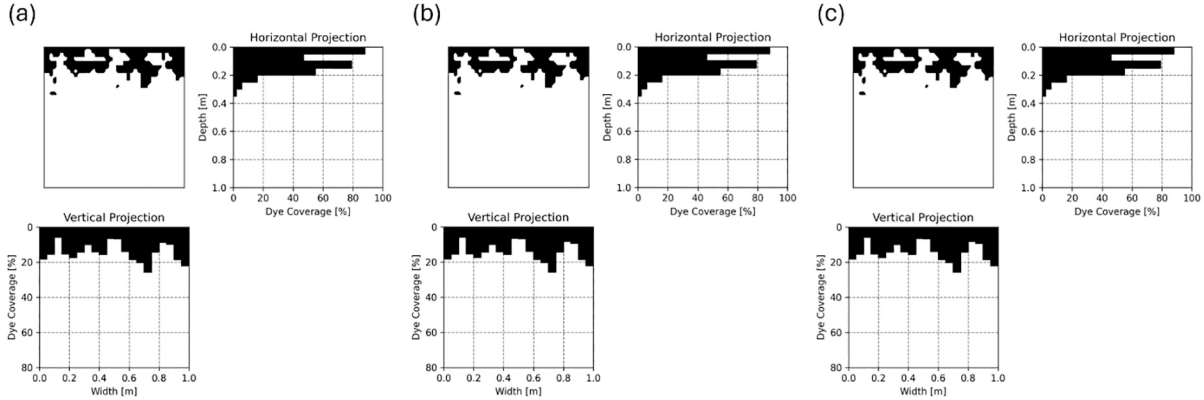

Fig. A3. Slices of the domain and their respective dye coverages to highlight the tracer activation region at 35 % degree of saturation when varying of Equation as (a) 509, (b) 500 (R2 reference value), and (c) 491

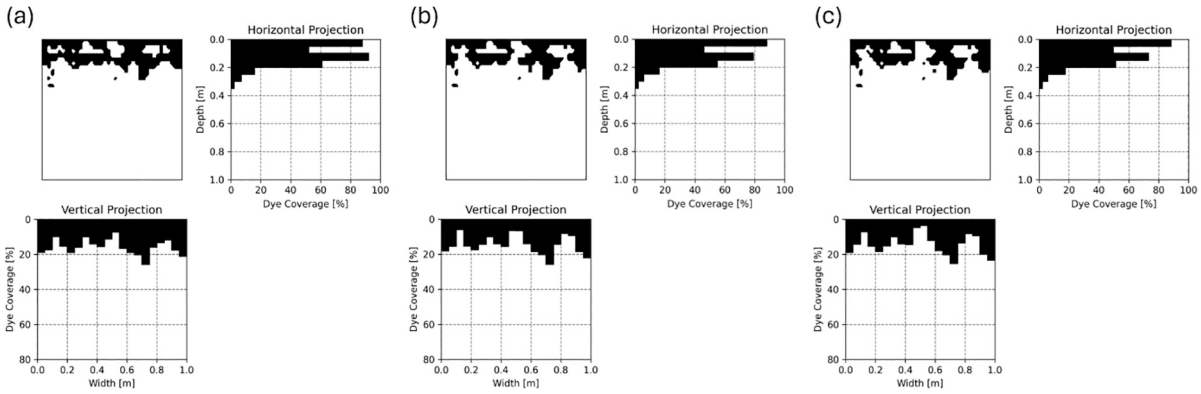

Fig. A4. Slices of the domain and their respective dye coverages to highlight the tracer activation region at 35 % degree of saturation when varying of Equation as (a) 1.15, (b) 1 (R2 reference value), and (c) 0.85

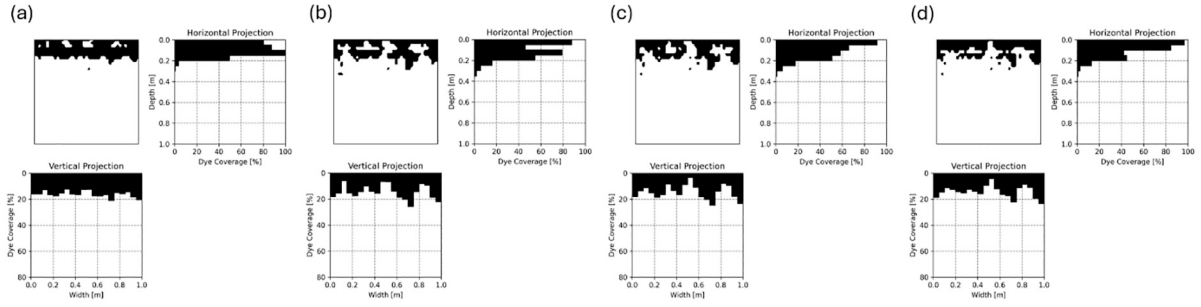

Fig. A5. Slices of the domain and their respective dye coverages to highlight the tracer activation region at 35 % degree of saturation when varying of Equation as (a) 0.1, (b) 0.2 (R2 reference value), (c) 0.3, and (d) 0.5

Appendix B

The following contains additional results from the analyses conducted in this study. For the full range of 800 slices, see: https://github.com/EJRicketts/HydrophobicSlices.

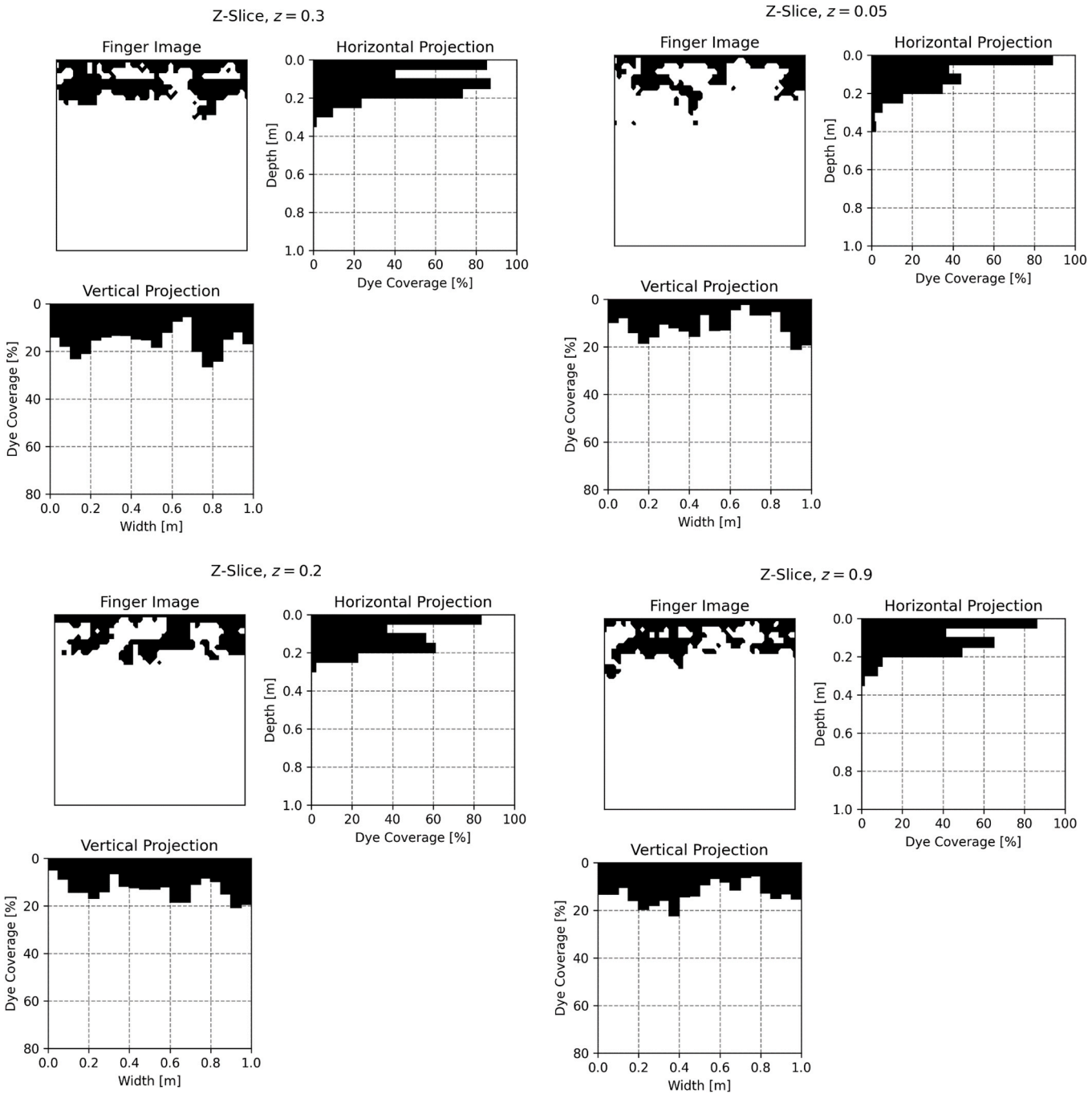

Fig. B1. Slices of the domain and their respective dye coverages to highlight the tracer activation region at 35 % degree of saturation

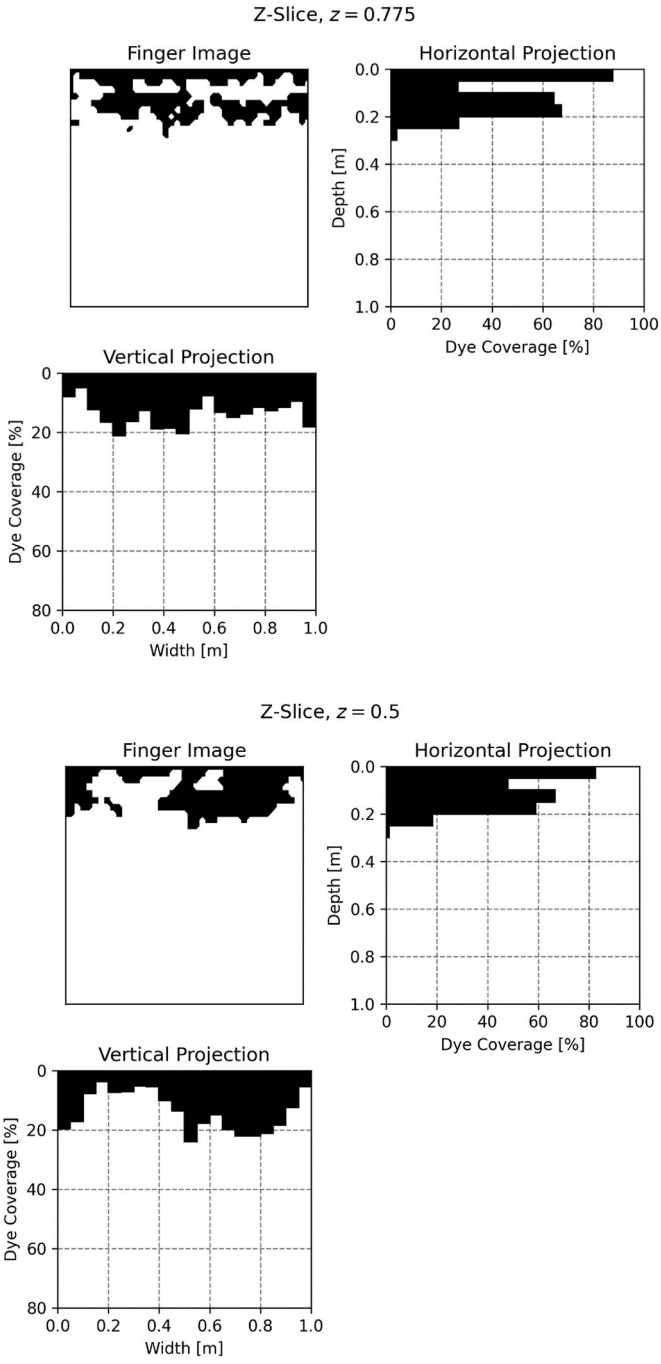

Fig. B1. (*continued*).

Appendix C

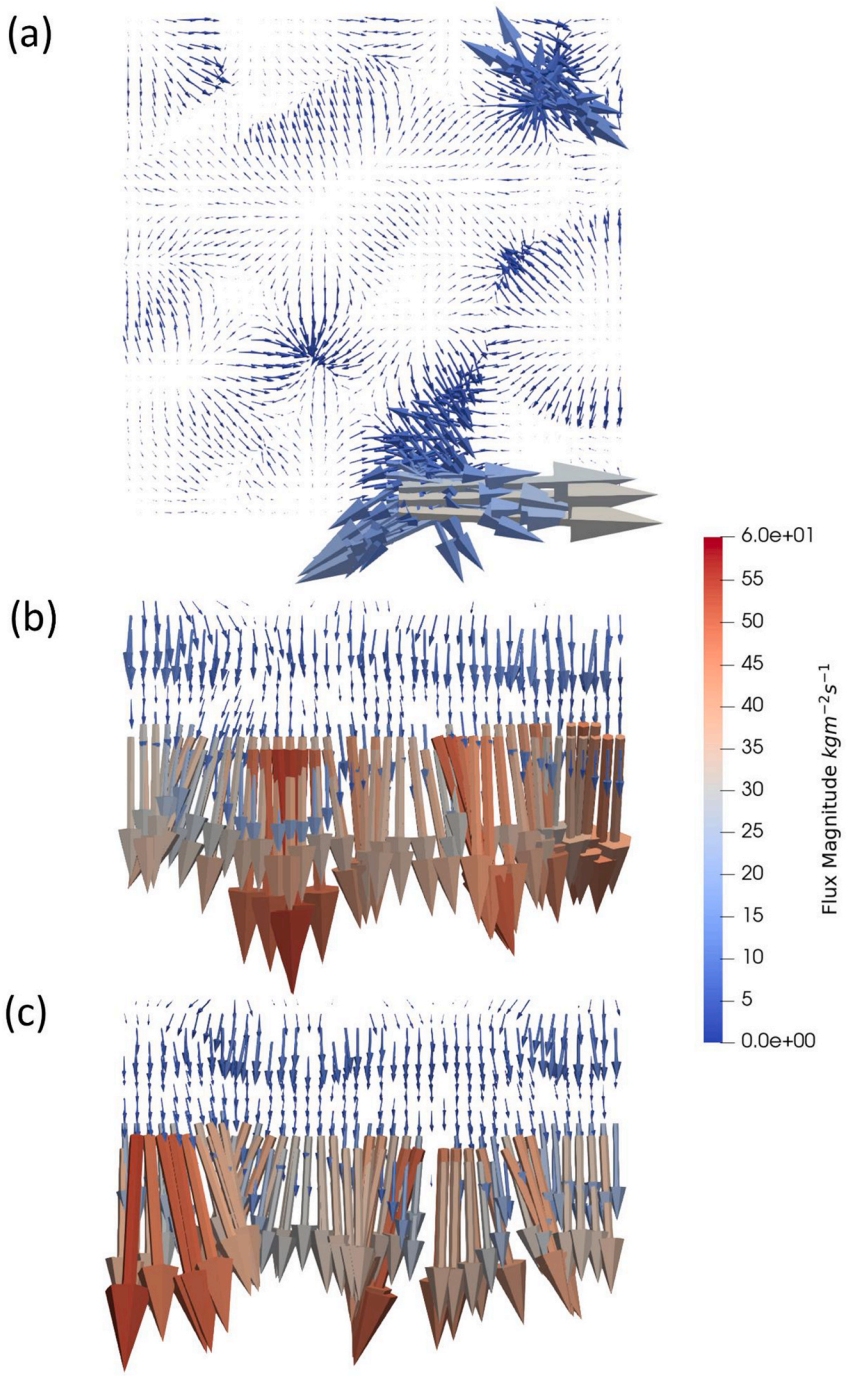

Fig. C1. Computation of the (a) lateral and (b-c) vertical flux profiles at 2.5 h, where (b) and (c) are perpendicular to each other

Data availability

Data will be made available on request.

References

Ahmadi, H., Namin, M.M., Kilanehei, F., 2016. Development a numerical model of flow and contaminant transport in layered soils. Adv. Environ. Res. 5 (4), 263–282. https://doi.org/10.12989/aer.2016.5.4.263.

Ahmed, M.A., Kroener, E., Benard, P., Zarebanadkouki, M., Kaestner, A., Carminati, A., 2016. Drying of mucilage causes water repellency in the rhizosphere of maize: measurements and modelling. Plant and Soil 407 (1–2), 161–171. http://link.springer.com/10.1007/s11104-015-2749-1.

Bachmann, J., McHale, G., 2009. Superhydrophobic surfaces: a model approach to predict contact angle and surface energy of soil particles. Eur. J. Soil Sci. 60 (3), 420–430. https://onlinelibrary.wiley.com/doi/10.1111/j.1365-2389.2008.01118.x.

Bardet, J.-P., Jesmani, M., Jabbari, N., 2014. Permeability and compressibility of wax-coated sands. Géotechnique 64 (5), 341–350. https://www.icevirtuallibrary.com/doi/10.1680/geot.13.P.118.

Bauters, T.W.J., Steenhuis, T.S., Parlange, J.-Y., DiCarlo, D.A., 1998. Preferential Flow in Water-Repellent Sands. Soil Sci. Soc. Am. J. 62 (5), 1185–1190. http://doi.wiley.com/10.2136/sssaj1998.03615995006200050005x.

Bodí, M.B., Doerr, S.H., Cerdà, A., Mataix-Solera, J., 2012. Hydrological effects of a layer of vegetation ash on underlying wettable and water repellent soil. Geoderma 191, 14–23. https://linkinghub.elsevier.com/retrieve/pii/S0016706112000286.

Brooks, R.H., Corey, A.T., 1966. Properties of Porous Media Affecting Fluid Flow. Journal of the Irrigation and Drainage Division 92 (2), 61–88. https://doi.org/10.1061/JRCEA4.0000425.

Cerdà, A., Doerr, S.H., 2008. The effect of ash and needle cover on surface runoff and erosion in the immediate post-fire period. Catena 74 (3), 256–263. https://linkinghub.elsevier.com/retrieve/pii/S0341816208000222.

Chitez, A.S., Jefferson, A.D., 2015. Porosity development in a thermo-hygral finite element model for cementitious materials. Cem. Concr. Res. 78, 216–233. https://doi.org/10.1016/j.cemconres.2015.07.010.

Cleall, P.J., Seetharam, S.C., Thomas, H.R., 2007. Inclusion of some aspects of chemical behavior of unsaturated soil in thermo/hydro/chemical/mechanical models. I: Model development. J. Eng. Mech. 133 (3), 338–347. https://ascelibrary.org/doi/10.1061/%28ASCE%290733-9399%282007%29133%3A3%28338%29.

Cremer, C.J.M., Schuetz, C., Neuweiler, I., Lehmann, P., Lehmann, E.H., 2017. Unstable Infiltration Experiments in Dry Porous Media. Vadose Zone J. 16 (7), vzj2016.10.0092. http://doi.wiley.com/10.2136/vzj2016.10.0092.

Cueto-Felgueroso, L., Suarez-Navarro, M.J., Fu, X., Juanes, R., 2020. Numerical simulation of unstable preferential flow during water infiltration into heterogeneous dry soil. Water 12 (3), 909. https://doi.org/10.3390/w12030909.

Darcy, H., 1856. *Les fontaines publiques de la vile de Dijon*. Dalmont, Paris.

DeBano, L.F., 2000. Water repellency in soils: a historical overview. J. Hydrol. 231–232, 4–32. https://linkinghub.elsevier.com/retrieve/pii/S0022169400001803.

Diamantopoulos, E., Durner, W., Reszkowska, A., Bachmann, J., 2013. Effect of soil water repellency on soil hydraulic properties estimated under dynamic conditions. J. Hydrol. 486, 175–186. https://doi.org/10.1016/j.jhydrol.2013.01.020.

Dou, Z., Liu, Y., Zhang, X., Wang, Y., Chen, Z., Wang, J. and Zhou, Z. 2021. Influence of Layer Transition Zone on Rainfall-Induced Instability of Multilayered Slope. *Lithosphere* 2021(SpecialIssue 4). doi: 10.2113/2021/2277284.

Foroughi, S., Bijeljic, B., Blunt, M.J., 2022. A closed-form equation for capillary pressure in porous media for all wettabilities. Transp. Porous Media. https://doi.org/10.1007/s11242-022-01868-3.

Gjettermann, B., Nielsen, K.L., Petersen, C.T., Jensen, H.E., Hansen, S., 1997. Preferential flow in sandy loam soils as affected by irrigation intensity. Soil Technol. 11 (2), 139–152. https://linkinghub.elsevier.com/retrieve/pii/S0933363097000019.

Glass, R.J., Steenhuis, T.S., Parlange, J.-Y., 1988. Wetting front instability as a rapid and far-reaching hydrologic process in the vadose zone. J. Contam. Hydrol. 3 (2–4), 207–226. s://linkinghub.elsevier.com/retrieve/pii/0169772288900320.

Granged, A.J.P., Jordán, A., Zavala, L.M., Bárcenas, G., 2011. Fire-induced changes in soil water repellency increased fingered flow and runoff rates following the 2004 Huelva wildfire. Hydrol. Process. 25 (10), 1614–1629. https://onlinelibrary.wiley.com/doi/10.1002/hyp.7923.

Heilig, A., Steenhuis, T.S., Walter, M.T., Herbert, S.J., 2003. Funneled flow mechanisms in layered soil: field investigations. J. Hydrol. 279 (1–4), 210–223. https://doi.org/10.1016/S0022-1694(03)00179-3.

Hopp, L., Peiffer, S., Durner, W., 2006. Spatial variability of arsenic and chromium in the soil water at a former wood preserving site. J. Contam. Hydrol. 85 (3–4), 159–178. https://doi.org/10.1016/j.jconhyd.2006.01.005.

Hosseinejad, F., Kalateh, F., Mojtahedi, A., 2019. Numerical Investigation of liquefaction in earth dams: a Comparison of Darcy and Non-Darcy flow models. Comput. Geotech. 116. https://doi.org/10.1016/j.compgeo.2019.103182.

Kawamoto, K., Miyazaki, T., 1999. Fingering flow in homogeneous sandy soils under continuous rainfall infiltration. Soils Found. 39 (4), 79–91. https://linkinghub.elsevier.com/retrieve/pii/S0038080620311094.

Li, D.Q., Xiao, T., Zhang, L.M., Cao, Z.J., 2019. Stepwise covariance matrix decomposition for efficient simulation of multivariate large-scale three-dimensional random fields. App. Math. Model. 68, 169–181. https://doi.org/10.1016/j.apm.2018.11.011.

Lindgren, F., Bolin, D., Rue, H., 2022. The SPDE approach for Gaussian and non-Gaussian fields: 10 years and still running. Spatial Stat. 50. https://doi.org/10.1016/j.spasta.2022.100599.

Lindgren, F., Rue, H., Lindström, J., 2011. *An explicit link between Gaussian fields and Gaussian Markov random fields: the stochastic partial differential equation approach*.

Lipsius, K., Mooney, S.J., 2006. Using image analysis of tracer staining to examine the infiltration patterns in a water repellent contaminated sandy soil. Geoderma 136 (3–4), 865–875. https://doi.org/10.1016/j.geoderma.2006.06.005.

Liu, C.-Y., Ku, C.-Y., Huang, C.-C., Lin, D.-G., Yeih, W.-C., 2015. Numerical solutions for groundwater flow in unsaturated layered soil with extreme physical property contrasts. Int. J. Nonlinear Sci. Numerical Simulation 16 (7–8), 325–335. https://doi.org/10.1515/ijnsns-2015-0060.

Lowe, M.-A., McGrath, G., Leopold, M., 2021. The impact of soil water repellency and slope upon runoff and erosion. Soil Tillage Res. 205, 104756. https://linkinghub.elsevier.com/retrieve/pii/S0167198720305389.

Montoya-Noguera, S., Zhao, T., Hu, Y., Wang, Y., Phoon, K.-K., 2019. Simulation of non-stationary non-Gaussian random fields from sparse measurements using Bayesian compressive sampling and Karhunen-Loève expansion. Struct. Saf. 79, 66–79. https://doi.org/10.1016/j.strusafe.2019.03.006.

Moradi, A.B., et al., 2012. Is the Rhizosphere Temporarily Water Repellent? Vadose Zone J. 11 (3), vzj2011.0120. http://doi.wiley.com/10.2136/vzj2011.0120.

Morris, C., Mooney, S.J., 2004. A high-resolution system for the quantification of preferential flow in undisturbed soil using observations of tracers. Geoderma 118 (1–2), 133–143. https://linkinghub.elsevier.com/retrieve/pii/S0016706103001897.

Mualem, Y., 1976. A new model for predicting the hydraulic conductivity of unsaturated porous media. Water Resour. Res. 12 (3), 513–522. https://doi.org/10.1029/WR012i003p00513.

Ng, S.H.Y., Lourenço, S.D.N., 2016. Conditions to induce water repellency in soils with dimethyldichlorosilane. Géotechnique 66 (5), 441–444. https://www.icevirtuallibrary.com/doi/10.1680/jgeot.15.T.025.

Nieber, J., Sheshukov, A., Egorov, A., Dautov, R., 2003. Non-equilibrium model for gravity-driven fingering in water repellent soils: Formulation and 2D simulations. In: *Soil Water Repellency*. Elsevier, pp. 245–257. Available at: https://linkinghub.elsevier.com/retrieve/pii/B9780444512697500254.

Nieber, J.L., 1996. Modeling finger development and persistence in initially dry porous media. Geoderma 70 (2–4), 207–229. https://linkinghub.elsevier.com/retrieve/pii/0016706195000860.

Nielsen, D.R., Th. Van Genuchten, M., Biggar, J.W., 1986. Water flow and solute transport processes in the unsaturated zone. Water Resour. Res. 22 (9S), 89S–108S. https://doi.org/10.1029/WR022i09Sp0089S.

Nyman, P., Sheridan, G.J., Smith, H.G., Lane, P.N.J., 2014. Modeling the effects of surface storage, macropore flow and water repellency on infiltration after wildfire. J. Hydrol. 513, 301–313. https://linkinghub.elsevier.com/retrieve/pii/S0022169414001528.

Reichenberger, S., Amelung, W., Laabs, V., Pinto, A., Totsche, K.U., Zech, W., 2002. Pesticide displacement along preferential flow pathways in a Brazilian Oxisol. Geoderma 110 (1–2), 63–86. https://linkinghub.elsevier.com/retrieve/pii/S0016706102001829.

Ricketts, E.J., Cleall, P.J., Jefferson, A., Kerfriden, P., Lyons, P., 2023a. Representation of three-dimensional unsaturated flow in heterogeneous soil through tractable Gaussian random fields. Géotechnique 1–13. https://www.icevirtuallibrary.com/doi/10.1680/jgeot.22.00316.

Ricketts, E.J., Cleall, P.J., Jefferson, A., Kerfriden, P., Lyons, P., 2024. Influence of spatially varying boundary conditions based on material heterogeneity. Eur. J. Computational Mech. 199–226. https://doi.org/10.13052/ejcm2642-2085.3331.

Ricketts, E.J., Cleall, P.J., Jefferson, T., Kerfriden, P., Lyons, P., 2023b. Near-boundary error reduction with an optimized weighted Dirichlet–Neumann boundary condition for stochastic PDE-based Gaussian random field generators. Eng. Comput. https://doi.org/10.1007/s00366-023-01819-6.

Ricketts, E.J., Freeman, B.L., Cleall, P.J., Jefferson, A., Kerfriden, P., 2023c. A Statistical Finite Element Method Integrating a Plurigaussian Random Field Generator for Multi-scale Modelling of Solute Transport in Concrete. Transp. Porous Media 148 (1), 95–121. https://link.springer.com/10.1007/s11242-023-01930-8.

Ritsema, C.J., Dekker, L.W., 2000. Preferential flow in water repellent sandy soils: principles and modeling implications. J. Hydrol. 231–232, 308–319. https://linkinghub.elsevier.com/retrieve/pii/S0022169400002031.

Ritsema, C.J., Dekker, L.W., Nieber, J.L., Steenhuis, T.S., 1998. Modeling and field evidence of finger formation and finger recurrence in a water repellent sandy soil. Water Resour. Res. 34 (4), 555–567. https://doi.org/10.1029/97WR02407.

Roininen, L., Huttunen, J.M.J., Lasanen, S., 2014. Whittle-matérn priors for Bayesian statistical inversion with applications in electrical impedance tomography. Inverse Probl. Imaging 8 (2), 561–586. https://doi.org/10.3934/ipi.2014.8.561.

Romano, N., Brunone, B., Santini, A., 1998. Numerical analysis of one-dimensional unsaturated flow in layered soils. Adv. Water Resour. 21 (4), 315–324. https://doi.org/10.1016/S0309-1708(96)00059-0.

Rosso, R., Rulli, M.C., Vannucchi, G., 2006. A physically based model for the hydrologic control on shallow landsliding. Water Resour. Res. 42 (6). https://doi.org/10.1029/2005WR004369.

Saulick, Y., Lourenço, S., 2020. Hydrophobisation of clays and nano silica for ground engineering. Cardoso, R., Jommi, C., and Romero, E. eds. *E3S Web of Conferences* 195, p. 03039. Available at: https://www.e3s-conferences.org/10.1051/e3sconf/202019503039.

van Genuchten, M.Th., 1980. A Closed-form Equation for Predicting the Hydraulic Conductivity of Unsaturated Soils. Soil Science Society of America Journal 44 (5), 892–898. https://doi.org/10.2136/sssaj1980.03615995004400050002x.

Wang, J.P., Zhuang, P.Z., Luan, J.Y., Liu, T.H., Tan, Y.R., Zhang, J., 2019. Estimation of unsaturated hydraulic conductivity of granular soils from particle size parameters. Water (Switzerland) 11 (9). https://doi.org/10.3390/w11091826.

Woods, S.W., Birkas, A., Ahl, R., 2007. Spatial variability of soil hydrophobicity after wildfires in Montana and Colorado. Geomorphology 86 (3–4), 465–479. https://doi.org/10.1016/j.geomorph.2006.09.015.

Zheng, S., Lourenço, S.D.N., Cleall, P.J., Ng, A.K.Y., 2019. Erodibility of synthetic water repellent granular materials: Adapting the ground to weather extremes. Sci. Total Environ. 689, 398–412. https://linkinghub.elsevier.com/retrieve/pii/S0048969719329018.

Zheng, S., Xing, X., Lourenço, S.D.N., Cleall, P.J., 2021. Cover systems with synthetic water-repellent soils. Vadose Zone J. 20 (1). https://onlinelibrary.wiley.com/doi/10.1002/vzj2.20093.

Zickenrott, I., Woche, S.K., Bachmann, J., Ahmed, M.A., Vetterlein, D., 2016. An efficient method for the collection of root mucilage from different plant species—A case study on the effect of mucilage on soil water repellency. J. Plant Nutr. Soil Sci. 179 (2), 294–302. https://onlinelibrary.wiley.com/doi/10.1002/jpln.201500511.

Zienkiewicz, O.C., Taylor, R.L. and Zhu, J.Z. 2013. *The Finite Element Method: its Basis and Fundamentals*. Elsevier. doi: 10.1016/C2009-0-24909-9.